

1 **Transport of Thermal-energy Ionospheric Oxygen (O^+) Ions between the Ionosphere and**
2 **the Plasma Sheet and Ring Current at Quiet Times Preceding Magnetic Storms**

3

4 Andrew W. Yau, Andrew Howarth

5 Department of Physics and Astronomy, University of Calgary, Calgary, Alberta, Canada

6

7 W.K. Peterson

8 Laboratory of Atmospheric and Space Physics, University of Colorado, Boulder, Colorado, USA

9

10 Takumi Abe

11 Institute of Space and Astronautical Science, Sagamihara, Kanagawa, Japan

12 Abstract

13 The presence of energetic O^+ ions in the ring current at the onset of a magnetic storm
14 prompts the question of the possible role of “in-transit” ionospheric O^+ ions between the
15 ionosphere and the plasma sheet and ring current in the quiet periods immediately preceding the
16 main phase of a magnetic storm. Thermal-energy O^+ ions are often observed in the quiet-time
17 high-altitude (>7000 km) polar ionosphere on Akebono, at temperatures of ~ 0.2 - 0.3 eV and flow
18 velocities of a few km/s. In this paper, we use single-particle trajectory simulation to study the
19 transport of these ions in the periods preceding a number of large magnetic storms ($Dst < -100$
20 nT). Our simulation shows that due to the centrifugal acceleration at higher altitudes (above ~ 3
21 R_E altitude), about 10-20% of polar wind and other low-energy O^+ ions reaches the plasma sheet
22 during such periods; the actual percentage is a factor of ~ 3 larger in the dusk sector on average
23 compared with the dawn sector and dependent on the IMF and the O^+ ion temperature. This
24 provides a low but non-negligible flux of O^+ ions between the ionosphere and the plasma sheet
25 and ring current, which is believed to constitute a significant “in-transit” oxygen ion population
26 over a period of a few (~ 4) hours preceding a magnetic storm. Such a population could explain
27 the presence of energetic O^+ ions at the onset of the main phase of the storm, when the heavy
28 ions could potentially modify the evolution of the ring current.

1. Introduction

The plasma in the ring current is believed to come primarily from the plasma sheet, which in turn originates from the solar wind and the ionosphere; see for example the comprehensive review of *Hultqvist et al.* [1999] on the sources and losses of plasma in different magnetospheric regions. Within the ring current plasma, the energetic O^+ ion population is believed to originate from the ionosphere, and to play an important role in the particle and magnetic field pressure distributions during a geomagnetic storm [*Fok et al.*, 2001; *Jordanova*, 2003, *Zaharia et al.*, 2006]. Since the latter are an integral part of the large-scale magnetospheric current system, the nature of energization and transport of the seed O^+ populations in the ionosphere is believed to be an important part of the ring current dynamics.

The outflow rate of energetic (> 10 eV) upflowing ionospheric O^+ ions is strongly dependent on both geomagnetic and solar activity levels [*Yau et al.*, 1985]. Using data from the DE-1 energetic ion composition spectrometer (EICS) between 16,000 and 24,000 km altitude, *Yau et al.* [1998] parameterized the observed *hemispherical* flux F of >10 -eV O^+ ions as a function of the solar radio flux and K_P indices. Explicitly, $F(K_P, F_{10.7}) = 5 \times 10^{24} \exp[0.01(F_{10.7} - 100)] \exp(0.50 K_P)$, and the hemispherical flux ranges from 3.7×10^{24} ions s^{-1} at $K_P = 0$, $F_{10.7} = 70$, to 2×10^{26} ions s^{-1} at $K_P = 9$, $F_{10.7} = 250$, corresponding to a range of 0.2–10 kg/s in O^+ mass outflow rate over the two hemispheres.

The thermal plasma density in the polar ionosphere is found to exhibit a significant variation with seasons, and to transition from an exponential altitude dependence at low altitude to a power-law relationship at high altitude up to at least $\sim 10,000$ km, i.e. $n_e = n_1 \exp(-z/h) + n_2 r^{-\alpha}$, where n_e is the median electron density, the coefficients n_1 , n_2 , h and α are a function of the season, invariant latitude and local time, and the power law and exponential terms equal each

other at the transition height (H_T) [Kitamura *et al.*, 2009]. Near solar maximum, the transition height varies from ~1500 km to ~4000 km and the plasma density (n_e) ranges from about 20 to 10^2 cm^{-3} above 6000 km altitude at equinox.

As discussed in Chappell *et al.* [1987] and Yau and Andre [1997], the polar wind constitutes a dominant component of the thermal plasma in the polar ionosphere, and it exhibits several “non-classical” features at high altitude, which are attributed to a number of ion acceleration mechanisms associated with strong ionospheric convection in regions of large magnetic field curvatures, enhanced electron and ion temperatures, and escaping atmospheric photoelectrons [Yau *et al.*, 2007]. At Akebono altitudes (<10,000 km), the observed polar wind is comprised mainly of H^+ , He^+ and O^+ ions, and electrons. The ions have an averaged ion temperature of ~0.2–0.3 eV [Drakou *et al.*, 1997], a day-night asymmetry in ion velocity (larger averaged velocity on the dayside), and a rate of increase in ion velocity with altitude that correlates strongly with electron temperature and varies with solar activity level [Abe *et al.*, 2004]. At a given altitude, the polar wind velocity is highly variable, and is on average largest for H^+ and smallest for O^+ .

O^+ ions often constitute a significant and at times dominant component of the thermal ion population, the observed O^+/H^+ ratio being in the range of 0.1–0.5 near solar maximum [Yau *et al.*, 1991] and in a lower range near solar minimum [Cully *et al.*, 2003a]. Thus, the observed O^+ polar wind at Akebono altitudes may be characterized by a cold, drifting plasma with a temperature of ~0.2–0.3 eV, a drift velocity of ~2–4 km/s and a seasonally-dependent density of a few to ~30 cm^{-3} near solar maximum, and it represents a non-negligible supply of escaping low-energy O^+ ions; note, however, that observationally it is not always possible to

unambiguously separate polar wind O⁺ ions from other low-energy ion populations, such as a low-energy “cleft ion fountain” ion that has convected into a polar wind flux tube.

Peterson et al. [2008] estimated the escaping hemispherical O⁺ ion flux and characteristic energy at ~6000 km at magnetically quiet times, by including both the energetic (0.015–17 keV) ion data from the torodial ion mass angle spectrograph (TIMAS) [*Lennartsson et al.*, 2004] and the thermal (0–50 eV) ion data thermal ion dynamics experiment (TIDE) [*Su et al.*, 1998] on Polar, and assuming uniform thermal ion flux throughout the auroral zone and polar cap and a characteristic energy of 1 eV in the thermal component. Near solar minimum, the estimated flux was $\sim 4.6 \times 10^{24}$ in the auroral region and 6.2×10^{24} ions s⁻¹ in the polar cap. The thermal component was estimated to constitute as much as ~63 and 99% in the two regions. Both the estimated flux and the assumed characteristic energy values are upper limits since the escaping thermal O⁺ ion flux is not spatially uniform and the polar wind typically has a characteristic energy below 1 eV.

The escape velocity v_e of a particle in the exosphere is determined by the kinetic energy required to overcome the Earth’s gravitational potential and is given by $v_e = (2 g_0 R_E^2 / r)^{1/2}$, where g_0 is the acceleration due to gravity at the Earth surface, R_E is the Earth radius, and r is the radial distance of the particle. Thus, v_e is ~11 km-s⁻¹ at the exobase (500 km altitude) and ~8 km/s at 1 R_E altitude independent of ion mass species. In comparison, the typical velocity of a polar wind O⁺ ion is much smaller (~2–4 km/s) near 1 R_E altitude, while the velocity of a cleft ion fountain O⁺ ion with a drift energy of 10-20 eV is larger (10 – 15 km/s). However, in the context of polar wind plasma transport, it is important to recognize that the escape velocity corresponds to the velocity that an ion needs to reach an infinite distance from Earth in the absence of any acceleration. The minimum velocity required for the ion to reach the

magnetosphere is often smaller, since the distance between the ionosphere and the magnetosphere is not infinite, and as noted above a number of acceleration mechanisms exist between the two.

To assess the possibility of the oxygen polar wind being a potential source of plasma sheet and ring current plasma, it is instructive to compare the observed O^+ density and temperature and the corresponding escaping fraction due to thermal Jeans escape at 500, 7000, and 50,500 km, which correspond to the exobase, the altitude of Akebono data in the present study, and the Polar apogee and the highest altitude of available polar wind data, respectively. The fraction of escaping particles in a drifting Maxwellian is given by $f_{esc} = [1 - \exp(-(v_e - v_d)^2/v_t^2)]^{1/2}$, where v_d and v_t are the particle vertical drift and thermal velocity, respectively; $v_d < v_e$, $v_t = (kT/m)^{1/2}$, and m and T are particle mass and temperature. At the exobase, where the O^+ density is typically $<10^5 \text{ cm}^{-3}$ and the temperature is typically 0.1 eV, the fraction of escaping O^+ ions is obviously negligible ($<10^{-80}$). At Akebono altitude where the temperature is ~ 0.2 to 0.3 eV and the parallel velocity is ~ 2 – 4 km/s, as noted above, the fraction of escaping ions is much less negligible although it remains much smaller than unity ($\leq 2 \times 10^{-6}$). More important, the density of $\leq 30 \text{ cm}^{-3}$ is clearly many orders of magnitude larger than the escaping density at the exobase, and reflects the effect of the overall polar wind acceleration in “lifting” a significant fraction of the plasma between the two altitudes.

Likewise, at Polar apogee, the observed O^+ density near solar minimum (0.05 cm^{-3}) [Su et al., 1998] is about 3 orders of magnitude larger than the escaping ion density ($\leq 6 \times 10^{-5} \text{ cm}^{-3}$) at Akebono altitude; the corresponding density near solar maximum is expected to be larger. The observed temperature (7.5 eV) and drift velocity (16.8 km/s) are also much larger, and imply the

occurrence of additional acceleration that is required to lift a sufficient fraction of the ions from the Akebono altitude to the Polar apogee.

Cully et al. [2003a] compared the observed magnitudes and $F_{10.7}$ and K_P dependences of low-energy H^+ and O^+ ion outflows on Akebono with those of energetic ion outflows on DE-1 and Polar, and found that the low-energy H^+ flow at Akebono altitude was entirely sufficient to account for the higher-energy flows at higher altitudes. In contrast, the low-energy O^+ flow could account for only a small fraction of the higher-energy flows at higher altitudes. In addition, both H^+ and O^+ outflow rates exhibited a strong correlation with the solar wind kinetic pressure, solar wind electric field, and interplanetary magnetic field (IMF) variability (δB_{IMF}) in the hour preceding hour. In particular, the rates exhibited a strong correlation with solar wind density and anti-correlation with solar wind velocity, independent of K_P .

Previous authors have used a number of single-particle trajectory tracing models to investigate the transport of ionospheric ions of various energies in the magnetosphere. Using a simple 2-dimensional model, *Cladis* [1986] demonstrated the importance of centrifugal ion acceleration in regions of curved or changing magnetic field. *Delcourt et al.* [1989, 1993, 1994] used both the guiding center and full equations of motion to study the 3-dimensional dynamics of auroral, polar cap, cusp and H^+ polar wind ions in different magnetospheric regions including the magnetotail. The H^+ polar wind was found to constitute a significant supply of H^+ ions to the plasma sheet particularly under magnetically quiet times, when the ions can reach further down tail under the influence of a weaker convection electric field and interact non-adiabatically in the plasma sheet.

Cully et al. [2003b] used the guiding center equations to address the question of auroral substorm trigger and the supply of various types of low-energy ions to the central plasma sheet

under both northward and southward IMF conditions, including both light (H^+) and heavy (O^+) polar wind and “cleft ion fountain” ions. It was found that a drastic northward turning of the IMF results in a reduced supply of O^+ ions to the near-tail region of the plasma sheet, where substorm onset is thought to originate. In addition, the low-energy O^+ ions often traverse along a field line for a long duration compared with the duration of magnetospheric reconfiguration during disturbed periods.

In a follow-on study, *Howarth and Yau* [2008] examined the influence of the IMF and convection electric field on the trajectories and destinations of polar wind and other low-energy ions observed on Akebono in the case of steady IMF and ionospheric convection. Ions were found to preferentially feed the dusk sector of the plasma sheet over the dawn sector when the IMF is duskward ($B_y > 0$), and to be more evenly distributed between the two sectors when the IMF is dawnward. It was also found that a larger percentage of O^+ ions originating from the noon or dusk sectors of the polar cap reaches the magnetosphere and beyond compared with ions from the dawn or midnight sectors, due to the increased centrifugal acceleration associated with the larger magnetic field curvature near noon and the larger convection electric field in the dusk sector. In addition, the O^+ outflow rate to both the plasma sheet and the magnetotail was found to correlate strongly with the ion temperature.

In a similar study, *Ebihara et al.* [2006] simulated the destination of suprathermal energy (14–209 eV) ionospheric O^+ ions observed on Akebono. This simulation used the full equation of motion and an empirical model of ion flux, which is based on K_p and the sunspot number and derived from Akebono suprathermal ion mass spectrometer (SMS) data. It assumed a source altitude of $1 R_E$ and time-independent external magnetic and convection electric fields using the Tsyganenko T89c [Tsyganenko, 1989] and Weimer W2K [Weimer 2001] models. Under an

active-time magnetic field and “mid-strength” convection electric field, the majority of O^+ ions that were above escape energy at the source altitude were found to reach the ring current, and only a very small fraction reached the magnetopause or the distant tail and the atmosphere. In comparison, under quiet-time conditions, the fraction of suprathermal ions reaching the ring current was a factor of 3 smaller, and the fractions reaching the magnetopause and the distant tail were a factor of 2 and 200 larger, respectively. In a subsequent case study of two geomagnetic storms using the same simulation code, *Kitamura et al.* [2010] found that some of the low-energy (a few eV) cleft ion fountain O^+ ions could also be transported to the ring current region during the storms.

Huddleston et al. [2005] extended the simulation code of *Delcourt et al.* [1993] to compute the full trajectories of H^+ and He^+ polar wind (0–3 eV) and cleft ion fountain (10–20 eV) ions, as well as O^+ cleft ion fountain and H^+ and O^+ auroral (500 eV) ions. A Volland electric field model with a Heelis correction was used in combination with ion measurements from the Polar TIDE instrument, and detailed trajectories were calculated for quiet and moderate levels of magnetic activity. An H^+ polar wind ion originating from the Polar perigee (5000 km) at auroral latitudes was often found to lose its kinetic energy initially but gradually gain energy at higher altitude due to “centrifugal acceleration”, as it experienced magnetic curvature drift through the convection electric field potential while convecting across the polar cap into the magnetospheric lobes. Thereafter, as the ion traversed the highly curved magnetic field in the neutral sheet, it was further and abruptly accelerated to “plasma sheet” energies of hundreds of eV. Thus, polar wind H^+ ions originating from or below auroral latitudes were interpreted as an important source of plasma sheet H^+ ions. In the case of the cleft ion fountain and auroral ions, the trajectories of different ion species originating from the same source location were found to

deviate from each other, with the heaviest ion species (O^+) reaching farthest down tail and the lightest ion species (H^+) least down tail.

In general, a geomagnetic storm has three phases: initial, main and recovery, and it can be classified as recurrent or non-recurrent. Recurrent storms, which occur most frequently in the declining phase of a solar cycle once every 27-day solar rotation, are believed to be triggered by a region of high solar wind pressure region formed by the interaction of low- and high-speed co-rotating solar wind streams. Non-recurrent geomagnetic storms, which occur most frequently near solar maximum, are believed to be triggered by a fast coronal mass ejection (CME) and the accompanying interplanetary shock wave. In both cases, a magnetic storm is often associated with the southward turning of the IMF, which results in an enhanced coupling between the IMF and the Earth's internal magnetic field; the enhanced coupling in turn intensifies the westward ring current and the induced southward magnetic field at the equator – and decreases the Dst in the main phase of a storm.

The initial phase, or storm sudden commencement (SSC), of a geomagnetic storm typically lasts 2 hours or longer and is characterized by an increase in the disturbance-storm time index (Dst) by up to about 50 nT, resulting from the compression of the magnetosphere due to the arrival of a CME, interplanetary shock, and/or sudden solar wind plasma pressure enhancement; not all geomagnetic storms have an initial phase, and not all SSC are followed by a geomagnetic storm. The main phase typically lasts several hours and is characterized by a decrease in Dst to a minimum value, which results from the intensification of the ring current and induced magnetic field at the equator, as noted above; the minimum Dst value is typically less than –50 nT, –100 nT, and –250 nT in the case of a “moderate”, “large”, and “super” storm, respectively. The recovery phase typically lasts up to a day or longer and is characterized by the

211 gradual increase in Dst to the pre-storm value, due to the gradual decay of the ring current
212 resulting from the loss of the current-carrying energetic charged particles to charge exchange and
213 other mechanisms.

214 In this paper, we extend the simulation model in *Howarth and Yau* [2008] to the case of
215 time-dependent magnetic and convection electric field, to study the transport of thermal-energy
216 polar wind O^+ ions in the quiet-time periods immediately preceding a number of large magnetic
217 storms. Our focus is on the time period immediately preceding the onset of the main phase of a
218 storm: this onset is identified as the time when Dst started to turn negative or to decrease sharply
219 in the case of a storm with and without an initial phase, respectively.

220 The organization of this paper is as follows. Section 2 briefly describes the trajectory
221 tracing model. Section 3 presents the simulated trajectories and magnetospheric destinations of
222 quiet-time polar wind O^+ preceding a number of magnetic storm events. Section 4 discusses the
223 feeding of these ions to the plasma sheet immediately preceding and at storm onset and the
224 resulting effects on the plasma sheet and the ring current in the main phase of the storm.

2. Particle Trajectory Simulation

The aim of the present simulation study is to determine the trajectories of polar wind O^+ ions in the high-altitude polar ionosphere in the quiet-time period preceding a magnetic storm, in order to determine their percentage (if any) and final energy and destination in the magnetosphere, and their overall possible effects on the plasma sheet and ring current. A total of five magnetic storms in 2000–2005 were selected for analysis; this period spanned the maximum and the early declining phase of Solar Cycle 23 (SC 23). In each case, simulation was performed for ions from different invariant latitude and MLT locations covering both the polar cap and the auroral zone, and starting at different initial velocities and different times preceding storm onset.

2.1 Simulation Model

The simulation model was adapted from *Cully et al.* [2003b] and *Howarth and Yau* [2008], and the simulation region encompasses the region of $X_{GSM} = +10$ to $-70 R_E$, $Y_{GSM} = -25$ to $+25 R_E$, and $Z_{GSM} = -30$ to $+30 R_E$. Starting at its source location $\mathbf{R}_0 (\equiv \mathbf{R}(t=t_0))$ and initial velocity $\mathbf{v}_0 (\equiv \mathbf{v}(t=t_0))$, the final destination of a particle can be determined by solving the full equation of motion:

$$\frac{d\vec{v}}{dt} = \frac{q}{m}(\vec{E} + \vec{v} \times \vec{B}) + \vec{G} \quad ; \quad \vec{G} = \frac{G_M M_E}{R^3} \vec{r} \quad (1)$$

In equation (1), q is the charge, m is the mass, and r is the radial distance of the particle from the Earth center; E is the electric field, B is the magnetic field, and G is the gravitational acceleration; G_M and M_E are the Earth's gravitational constant and mass, respectively. However, it is often computationally time-consuming to solve equation (1) for a large number of single particles due to the large amount of computations required to follow the gyro-motion of each particle as it traverses the magnetosphere. Under adiabatic conditions, where the electric and

magnetic fields do not vary significantly over a gyro-period or gyro-radius, it is sufficient to use the first-order guiding center equations of motion [Northrop, 1963]:

$$\frac{d v_{\parallel}}{dt} = G_{\parallel} + \frac{q}{m} E_{\parallel} - \frac{\mu}{m} \nabla_{\parallel} B + \vec{v}_{\vec{E} \times \vec{B}} \cdot \frac{d \hat{B}}{dt} \quad (2)$$

$$\vec{v}_{\perp} = \frac{\vec{E} \times \vec{B}}{B^2} + \frac{\mu}{q B^2} \vec{B} \times \nabla B + \frac{m}{q B^2} \vec{G} \times \vec{B} - \frac{m}{q B^2} \left[v_{\parallel} \frac{d \hat{B}}{dt} + \frac{d \vec{v}_{\vec{E} \times \vec{B}}}{dt} \right] \times \vec{B} \quad (3)$$

In equation (2) and (3), μ is the magnetic moment, the last term in (2) is the centrifugal acceleration term first discussed by Cladis [1986], and the time derivatives are convective derivatives and they depend on both time and space, i.e.

$$\frac{d}{dt} A = \left[\frac{\partial}{\partial t} + v_{\parallel} \nabla_{\parallel} + (\vec{v}_{\vec{E} \times \vec{B}} \cdot \nabla) \right] A \quad (4)$$

In order to trace the trajectories of a statistically significant number of particles, the guiding center equations (2-3) were used in the present study, except in the non-adiabatic regions of the plasma sheet and ring current in Figure 3 where the full equation (1) was used instead; in these regions, the ratio of the minimum field-line curvature encountered by an ion to the maximum ion gyro-radius in a time-step is expected to be small (<10). A fifth-order Runge-Kutta integration method was used to obtain the numerical solution in both cases.

The magnetic field was determined from a superposition of the Internal Geomagnetic Reference Field (IGRF) [Finlay, *et al.*, 2010], and the Tsyganenko 1996 (T96) external magnetic field model [Tsyganenko, 1995; Tsyganenko and Stern, 1996], which is parameterized by the Dst index and the Earth's dipole tilt angle, as well as instantaneous values of the solar wind dynamic pressure and IMF B_y and B_z ; the latter values were derived by time-shifting the solar wind measurements on ACE based on the satellite position (X_{GSM}) and measured solar wind velocity.

The electric field was determined in two steps. The electric field potential at the ionospheric level was first inferred from SuperDARN ion convection velocity data, and from the Applied Physics Lab statistical model [Ruohoniemi and Greenwald, 1996; Shepherd and Ruohoniemi, 2000] in the case of data gaps. The potential distribution was then mapped along the field lines to simulate the electric field at higher altitudes, by assuming the absence of parallel electric field (i.e. $E_{\parallel} = 0$), everywhere in the magnetosphere. This assumption is justified [Howarth and Yau, 2008] since the ambipolar electric field in the polar wind is typically less than 10^{-7} V m^{-1} and much smaller than the perpendicular convection electric field E_{\perp} in the simulation region ($>7000 \text{ km}$ altitude).

To expedite the computation, a non-uniformly spaced grid of $101 \times 101 \times 101$ grid points was used in which the grid spacing varied with the radial distance at a grid point from a minimum of $\sim 1/3 R_E$, and both the electric and magnetic fields at each grid point were pre-computed and updated every 10 minutes in response to the changing solar wind dynamic pressure and IMF. During the particle tracing, the E and B values at any position and time were obtained from the corresponding values at the nearest grid points in the nearest updates using linear interpolation in time and in space.

2.2 Particle Trajectories and Destinations

Starting at 4 hours or more before the onset in each storm, a total of 10,000 ions were “launched” from an altitude of 7000 km every 10 minutes. To ensure a statistically representative sampling of the large region of phase space, a Monte Carlo technique was used to randomly select the initial position (between 70° and 86° invariant and at all MLT) and velocity for each ion.

The Monte Carlo position selection assumed uniform ion density at all invariant latitudes above 70° and all MLT. The random velocity selection assumed a drifting Maxwellian velocity distribution with an ion temperature of 0.25 eV, a perpendicular velocity derived from the SuperDARN convection electric field data, and a parallel drift velocity derived from the observed polar wind O^+ velocity distribution between 6000 and 8000 km altitude [Abe *et al.*, 2004] as shown in Figure 1, as a function of the selected invariant latitude and MLT location.

The trajectory of each ion was followed until it reached one of 9 possible final destinations, and the initial and final position and velocity of each ion were captured for analysis. An ion was identified as “trapped” in the *atmosphere* if it was gravitationally trapped, descended below 600 km, or was below $1 R_E$ altitude after two hours. An un-trapped ion could convect to the *dayside* equatorial plane; reach the *magnetopause* or its vicinity where the field lines did not connect back to the ionosphere in the T96 model; flow to the *distant tail* beyond $X_{GSM} = -70 R_E$; cross the Plasma Sheet Boundary Layer (PSBL) tail-ward of $X_{GSM} = -15 R_E$ into the *dawn tail* or *dusk tail*; cross the PSBL earthward of $-15 R_E$ into the *dawn plasma sheet* or *dusk plasma sheet*; or flow out of the simulation region altogether.

Following Howarth and Yau [2008], the PSBL was defined as a function of the dipole tilt angle, and serves as the cutoff where the ions begin to experience non-adiabatic energization in the plasma sheet. In test simulation runs, the guiding center solution for none of the ions was found to deviate appreciably from the full solution at the cutoff, indicating that the ions remained adiabatic. Also, only a small fraction of a percent of the ions was found to flow out of the simulation region. This fraction of ions is excluded from the analysis below, which will focus on the other 8 ion destinations, including the atmosphere for the trapped ions and the 7

311 magnetospheric regions for the non-trapped ions: the dayside, magnetopause, distant tail, dawn
312 and dusk tail, and dawn and dusk plasma sheet.

3. Distribution of Particle Destinations

Relevant solar wind, IMF, and SuperDARN ion convection data were available for the five magnetic storms selected for analysis in the present study. These five storms spanned the period of 2000–2005 and the maximum and declining phases of SC 23, as well as the different seasons.

3.1 6 April 2000 Event

Figure 2 shows the geomagnetic and solar wind conditions preceding and during the 6 April 2000 storm, including (a) the 3-hr K_P index, (b) 1-min symmetric disturbance field in the horizontal component SYM-H, and the time-shifted solar wind data from ACE, including (c) the solar wind dynamic pressure P_{dyn} , (d) IMF B_Y and (e) B_Z . The rapid decrease in SYM-H starting near 1645 UT coincided with the sudden, ten-fold increase in the solar wind dynamic pressure, and the southward turning of the IMF, which resulted in the decrease of B_Z from about -2 nT to -20 nT. The rapid decrease signaled the onset of the main phase at this time. Note that the SYM-H is essentially the same as the Dst index [*Sugiura and Poros, 1971*] and that the time shift in the solar wind data is based on the measured solar wind velocity at ACE and is therefore subject to some uncertainty. In the immediately preceding quiet-time period, K_P increased from 3 at 1200 UT to 6 at 1500 UT. The IMF was initially weakly southward ($B_Z \approx$ a few nT negative) and then turned northward around 1430 UT while B_Y was small and downward (negative). During the main phase of the storm, K_P reached a maximum value of 8, and SYM-H reached a minimum value of about -320 nT near 0010 UT.

Figure 3 shows representative examples of simulated O^+ ion trajectories for this event, using the guiding-center (equations 2–3) and full equations of motion (equation 1) in the adiabatic and non-adiabatic regions, respectively. Figure 3a shows trajectories for ions starting at

1300 UT and originating at 75° invariant and 12 MLT, with initial energies of (a) 0.5, (b) 1.0, (c) 1.5, (d) 2.0, and (e) 3.0 eV, respectively. In this figure, the color of each trajectory trace denotes the initial ion energy. Each trajectory is projected onto the equatorial ($X_{GSM}-Y_{GSM}$) and noon-midnight ($X_{GSM}-Z_{GSM}$) plane. The lowest-energy ions followed trapped trajectories as they did not have sufficient energy to overcome gravitation before reaching the centrifugal acceleration altitude. In contrast, the higher-energy (2 and 3 eV) ions were able to reach the centrifugal acceleration altitude, where they started to gain energy. The highest-energy (3-eV) ion crossed the PSBL and reached the dusk plasma sheet farther down tail compared with the 2-eV ion.

Figure 3b shows the energy evolution of the 2- and 3-eV ions along their respective trajectories in the adiabatic region. In this figure, the instantaneous ion energy in each case is color-coded in logarithmic scale as the ion traversed from the starting location at 7000 km altitude to the PSBL. In the case of the 3-eV ion, the ion energy initially decreased to near 1 eV as the trajectory trace changed in color gradually from purple/red to blue. However, the energy stopped decreasing and instead started to increase as the ion reached higher altitude, to ~ 2.5 and >5 eV by the time the ion reached ~ 3 and $5 R_E$ altitude ($Z_{GSM} \sim 4$ and $6 R_E$), respectively; correspondingly, the trajectory trace changed from purple/red at $3 R_E$ to orange at $5 R_E$ altitude. The ion energy eventually reached 40 eV (and the trace changed to yellow) by the time the ion reached $X_{GSM} = -20 R_E$. In comparison, the 2-eV ion reached the PSBL at a closer distance ($X_{GSM} \sim -15 R_E$), and at a much lower energy (<5 eV). The difference between the two cases may be attributed to the dependence of the magnitude of ion acceleration on the parallel ion velocity in equation 4.

Figure 3c compares the trajectories of 2-eV ions originating from 4 different locations: (a) 80° invariant, 12 MLT; (b) 75° invariant, 12 MLT; (c) 75° invariant, 10 MLT; and (d) 75°

359 invariant, 14 MLT. In this figure, the color of each trace denotes the originating location. Note
 360 that the second of these four trajectories is the same as trajectory (d) in Figure 3a. Compared
 361 with the ion in this trajectory the other ions traversed regions of smaller magnetic field curvature
 362 as they traveled upward along the field line, and consequently experienced lesser centrifugal
 363 acceleration. Also, the two ions originating at 10 and 14 MLT (c and d) traversed primarily the
 364 dawn and dusk portions of the magnetosphere, respectively, while the ion originating from 75°
 365 invariant at 12 MLT (b) followed a predominantly noon-midnight trajectory. In comparison, the
 366 ion originating from 80° invariant experienced the least amount of centrifugal acceleration, and
 367 its trajectory was confined to a small radial distance at all times.

368 The guiding-center equation of motion (equations 2 and 3) was used exclusively in the
 369 trajectory calculations in Figure 4–8. Figure 4 shows the distribution of ion destinations as a
 370 function of the launch time of the ions before and during the storm, starting at 1250 UT, about 4
 371 hours before the storm onset at ~1645 UT. This figure shows the percentage of non-trapped ions
 372 arriving at each of the 7 destinations in the magnetosphere (color traces), and the total percentage
 373 of non-trapped ions (black trace). As noted in Section 2.2 above, a total of 10,000 ions were
 374 launched every 10 minutes, so that 240,000 ions were launched in all over a 4-hr period between
 375 1300 and 1700 UT. Slightly under 35–40% of the ions launched before 1500 UT was un-trapped,
 376 when K_p was 3, and the percentage increased slightly to ~40–45% between 1500 and 1800 UT,
 377 when K_p increased to 6; see Figure 2 above. About 7–16% of the ions launched before the onset
 378 (1645 UT) reached the dusk plasma sheet (dark blue), while about 3–8% of the ions reached the
 379 dawn plasma sheet (purple). The corresponding fractions of ions reaching the dusk and dawn
 380 sectors of the tail (gold and red) were comparable and the fractions reaching the dayside and the
 381 magnetopause (brown and green) were smaller in comparison. In other words, in the 4-hr quiet-

time period immediately preceding the start of this storm about 10 to 24% of the polar wind O^+ ions originating from 7000 km altitude was found to reach the plasma sheet.

Ions launched at a given time and source altitude generally arrive at their respective destinations at different times, since the travel time of each O^+ ion from its source location to its destination varies with its initial ion position and velocity, and depends on the geomagnetic and solar wind conditions, both of which affect the overall ion convection and ion trajectory. This can be seen in Figure 5, which shows the number of ions arriving at each destination as a function of the arrival time of the ions at the destination, irrespective and instead of the launch time of individual ions. Thus, for example, the distribution at 1500 UT includes ions launched at 1300 UT that had a travel time of 2 hr, as well as those launched at 1340 UT that had a travel time of 2 hours and 20 minutes, in other words ions launched 20 minutes earlier and traveling for 20 minutes longer. In this figure, each of the 7 color traces denotes the same destination as in Figure 4, but in contrast to Figure 4, the black trace denotes the number of trapped ions in the atmosphere instead of the total number of un-trapped ions in the 7 magnetospheric destinations.

Figure 5 shows a gradual build-up of the number of trapped ions before 1540 UT and a gradual decrease after 2100 UT, which reflect the increasing accumulation of ions launched starting at 1240 UT and the cessation of ion launch at the end of the simulation, respectively. As explained in Section 2.2 above, an ion is identified as “trapped” in the *atmosphere* if it was gravitationally trapped or if it descended below 600 km or was below 1 R_E altitude after two hours. Figure 5 also shows a sharper decrease in the percentage of trapped ions and sharper increase in the percentage of un-trapped ions compared with Figure 4 immediately before the storm onset. The sharper decrease in the trapped ion percentage reflects the increasing fraction of

ions being accelerated and becoming un-trapped as the strength of convection electric field increased with time in the period immediately before the storm onset.

By the time of the storm onset (1645 UT), more than 10% of the ions were un-trapped and reached the different regions of the magnetosphere. The number of ions reaching the dusk and dawn plasma sheet (dark blue and purple traces) peaked around 1900 UT, about 2 hours after the storm onset; at this time, the ratio of un-trapped ions reaching the plasma sheet to trapped ions in the atmosphere was about 0.45. This implies that about 20% of the polar wind O^+ ions launched a few hours earlier had reached the plasma sheet by this time.

The green trace in Figure 5 denotes the number of ions that “hit the magnetopause”, including (as explained in Section 2) ions that reached the magnetopause or its vicinity, where the field lines did not connect back to the ionosphere in the Tsyganenko 1996 (T96) model. This trace exhibits a sharp spike at the time of arrival of the solar wind pressure pulse at 1645 UT; cf. Figure 2. A detailed analysis of the simulation results shows the sudden compression of the magnetosphere at this time, when the magnetopause was pushed inward (earthward) by more than $1 R_E$ within the time interval between successive electric and magnetic field updates in the simulation (10 minutes). This resulted in the ions that were in the vicinity (within $1 R_E$) of the magnetopause in the different magnetospheric regions suddenly finding themselves arriving at or inside the magnetopause as the magnetosphere compressed suddenly – and hence a sudden increase in the number of ions that are designated as “hitting the magnetopause”.

To examine the detailed characteristics of the simulated O^+ ions that reached the plasma sheet and the magnetotail, Figure 6 shows the spatial and energy distributions of these ions as a function of X_{GSM} and Y_{GSM} . Each dot (data point) in this figure denotes an ion that was launched during the 8-hr simulation period (1250 – 2050 UT) and subsequently reached the plasma sheet

or magnetotail; the position of each dot denotes the X_{GSM} and Y_{GSM} coordinates of the ion while its color represents the ion energy.

A total of about 148,000 ions (about 31% of the 480,000 ions launched) are shown in Figure 6, and the density of the data points in the figure depicts qualitatively the spatial distribution of the simulated O^+ ions, which is expected to approximate the corresponding ion density distribution, given the nature of the Monte Carlo selection of initial particle phase space. Thus, it can be seen that the ion density in the plasma sheet was higher than that in the magnetotail, and that in both regions, the density was higher in the dusk sector.

Likewise, the dominant color in the respective areas of Figure 6 depicts the averaged ion energy in the different regions of the plasma sheet and magnetotail. Thus, it can be seen that the averaged ion energy of the O^+ ions increased with decreasing $|X_{GSM}|$, and that the ions reached keV energy as they crossed the PSBL. In addition, the ions along or near the midnight meridian ($|Y_{GSM}| < 5 R_E$) tended to have higher energies than those further away from the meridian ($|Y_{GSM}| > 5 R_E$). This trend is consistent with the pattern of less ion acceleration away from the magnetic local noon in Figure 3c above.

3.2 Comparison of Storms

Figures 4–6 show that in general a variable but non-negligible fraction of thermal-energy O^+ ions can become un-trapped and reach the magnetosphere in the period immediately before the onset of the main phase of a magnetic storm. The distribution of such un-trapped ions in the different regions of the magnetosphere is expected to be dependent on the prevailing geomagnetic and solar wind conditions. To examine this dependence in the five storms in the present study, Figure 7 shows (a) the 3-hr K_p index, (b) 1-min SYM-H, and time-shifted (c) solar wind dynamic pressure, P_{dyn} , (d) IMF B_Y and (e) B_Z from ACE preceding and during the five

storms: these storms occurred on (A) 6 April 2000, (B) 6 November 2000, (C) 5 November 2001, (D) 29 May 2003, and (E) January 21 2005, respectively. To facilitate data comparison, the data for the five storms are shown in different colors in each data panel, and offset with respect to the onset time of the main phase of each storm, i.e. the time when Dst started to turn negative or to decrease sharply in the case of a storm with and without a SSC, respectively.

Table 1 summarizes the time of storm onset, the minimum Dst (SYM-H) value, and the time of rapid increase and the maximum value of solar wind dynamic pressure (P_{dyn}) in each of the 5 storms studied (columns 3 to 6), as well as the range of IMF B_Y and B_Z in the 4-hr period following and preceding the onset, respectively (columns 7 to 10), for comparison with the distribution of ion destinations in the magnetosphere in each storm, including the percentage of ions that reached the dusk and dawn plasma sheet and tail, respectively (columns 11 to 14).

The first three of the five storms (storms A to C) were near the maximum phase of SC 23, while the remaining two (storms D and E) occurred in the declining phase of the cycle; as noted earlier, non-recurrent magnetic storms occur most frequently at solar maximum, while recurrent storms occur most frequently in the declining phase of a solar cycle. Together, the five storms spanned the four seasons of the year, occurring in spring, late fall, late fall, early summer, and late winter, respectively.

Based on the criterion of the minimum Dst value of a “moderate”, “large”, and “super” storm being less than -50 nT, -100 nT, and -250 nT, respectively, the five storms include a “moderate” storm with a minimum Dst of ~ -100 nT (storm E) and two “super-storms” with a minimum Dst below -320 nT (storms A and C), the other two storms (storms B and D) being “large” storms with a minimum Dst of ~ -170 nT. The first three storms (storms A to C) are identified as isolated storms in that Dst was above -50 nT for several hours immediately

preceding the storm in each case. Storm E is also treated as an isolated storm for the purpose of this study despite the very brief excursion of SYM-H to a value near -50 nT within an hour of the onset. In contrast, storm D appears to consist of a sequence of three overlapping storms with the second and third onset 4:40 and 5:30 after the first onset, respectively, and the three storms had minimum Dst values of -80 , -100 , and -170 nT, respectively.

In the context of thermal-energy plasma transport in the period immediately preceding the main phase of a storm, a number of differences in the geomagnetic and solar wind conditions are noteworthy between the five storms, including those in Figure 7 and Table 1. First, the initial phase (SSC) was present before the onset of the main phase of the storm in the case of storms A, C, and E, and possibly also D; in all four cases, Dst increased to 10 – 20 nT, and the value of AE was <1000 nT (not shown). In contrast, in the case of storm B, Dst remained negative and below -30 nT for several hours immediately before the storm onset; in this case, the AE index was much larger and exceeded 3000 nT in the 4-hr period before the onset, and was indicative of strong substorm activities.

Second, the onset of the main phase did not always coincide with the sudden enhancement in solar wind dynamic pressure and the southward turning of the IMF. Table 1 shows that the onset approximately coincided with the sudden rise in P_{dyn} in the case of storm A, but the two events were almost an hour apart in storm E. Data of P_{dyn} was not available at the time of onset in storm C. In the case of storm D, in which successive onsets occurred at 1700, 2140, and 2230 UT, three successive rises in P_{dyn} were observed at 1610, 2120, and 2240 UT. In other words, the last two onsets were within 15 minutes of the corresponding rise in P_{dyn} while the first onset and P_{dyn} rise were about 50 minutes apart.

Third, the minimum Dst ranged from ~ -100 to -320 nT while the maximum solar wind dynamic pressure during the main phase ranged from ~ 5 to 85 nP; note that in Figure 7, P_{dyn} is displayed in half scale (as $0.5 \times P_{dyn}$) in the case of storm E in order to make the data for the other storms more legible.

Fourth, both the B_Y and B_Z components of the IMF were quite variable in some of the storms in the 4-hr periods immediately preceding and following the onset, which, as noted above, did not coincide with the southward turning of the IMF in every storm. IMF was predominantly southward (B_Z was negative) most but not all of the time both before and after the onset in storm A (black trace in Figure 7). In contrast, it was highly variable in polarity but on balance northward (B_Z was positive) before the onset in storm B and E; in the case of storm E, the level of activity was moderate (Dst ~ -100 nT) despite the large solar wind dynamic pressure ($P_{dyn} = 85$ nP); this may perhaps be attributed to the mostly northward IMF at the time of solar wind pressure enhancement. In storm D, it was mostly northward before the first onset at 1700 UT, but underwent several changes in direction afterwards.

Fifth, the B_Y component of the IMF was predominantly dawnward (negative) and duskward (positive) in storm A and C, respectively, before the onset, and it remained predominantly dawnward for the first hour after the onset in storm A, when its magnitude increased from less than 5 nT to ~ 20 nT; solar wind particle data was not available for the determination of P_{dyn} and the time-shifting of the IMF data after the onset in storm C. In contrast, B_Y was variable before the onset in storms B, D, and E, and remained variable after the onset in storm D and E but became predominantly duskward (positive) in storm B.

Figure 8 compares the distribution of thermal-energy O^+ ions in the (a) plasma sheet and (b) magnetotail in the five storms. As in Figure 7, the data for the different storms are shown in

different colors and with respect to the onset time of the main phase of each storm. In each panel, the percentage of ions reaching the dusk and dawn sector is shown separately, with and without the solid circles, respectively, and as a function of the launch time of the ions, 0–4 hrs before the storm onset except in the case of storm C.

Note that in the simulation, ions that were gravitationally trapped or otherwise remained below 1 R_E altitude after 2 hours were identified as “trapped”, and most of the “un-trapped” ions reached their magnetospheric destinations within 4 hours after their launch. Therefore, in general, IMF and solar wind parameter data were required for the 4-hr period after the time of an ion launch, to update the electric and magnetic field distributions for the purpose of computing the ion trajectory. In the case of storm C, where the required solar wind plasma pressure data for the simulation was available only before the onset, the IMF and solar wind parameters were assumed to remain unchanged in the first 2 hours after the onset, and the data is displayed for ions launched 2–6 hrs before the onset and shifted to the right by 2 hours in the figure. In other words, the computed distributions for ions launched between 4 and 2 hours before the onset of storm C are shown on the right half of the green traces (between –02:00 and 00:00) in Figure 8, and they are believed to be approximate and may be in error due to variations in IMF and P_{dyn} in the first two hours after the onset.

Figure 8 shows that in all five storms, a variable percentage of the thermal-energy O^+ ions that were launched in the quiet-time period immediately preceding the storm onset reached the dawn and dusk plasma sheet and magnetotail. The percentage varied from ~20% to 39% and averaged to about 24–36% within each of the five storms studied. The percentage in the plasma sheet was ~30–40% larger than that in the magnetotail in storms A and B, and about 10–45%

540 smaller in the other three storms (C, D and E). In other words, about 17–21% of the ions reached
541 the plasma sheet in storms A and B and compared with 9–15% in storms C, D and E.

542 A dawn-dusk asymmetry in favor of the dusk sector is apparent in four of the five storms:
543 the dusk-to-dawn percentage ratio ranged from ~ 1.7 in storms A, B and D to 4.9 in storm E in
544 the plasma sheet, and from ~ 1.8 in storms A and D to 7.3 in storm E in the magnetotail.

545 The differences between the storms in their respective percentages of ions reaching
546 different regions of the magnetosphere may be attributed to a number of factors. First, the overall
547 percentage of un-trapped ions is expected to depend crucially on the magnitude of centrifugal ion
548 acceleration below the “turnaround” altitude, where an $\underline{\mathbf{E}} \times \underline{\mathbf{B}}$ convecting ion with less than escape
549 velocity will lose all of its initial kinetic energy to gravitation and fall back to the atmosphere in
550 the absence of any acceleration. It can be seen in equation 2 and 4 that for an $\underline{\mathbf{E}} \times \underline{\mathbf{B}}$ convecting
551 ion, the amplitude of ion acceleration due to a changing magnetic field increases with increasing
552 $\underline{\mathbf{E}} \times \underline{\mathbf{B}}$ velocity and/or increasing changes to the magnetic field in the $\underline{\mathbf{E}} \times \underline{\mathbf{B}}$ direction. This implies
553 that an increase in the amplitude of the IMF B_Y and B_Z components would result in an increase
554 in the overall amplitude of convection electric field, particularly under southward IMF
555 conditions [*Shepherd and Ruohobiemi, 2000*], and lead to larger centrifugal acceleration of the
556 thermal-energy ions below the turnaround altitude and ultimately a larger percentage of ions
557 being able to reach the different regions of the magnetosphere. Likewise, for a given $\underline{\mathbf{E}} \times \underline{\mathbf{B}}$
558 convection strength, the percentage of un-trapped ions is expected to increase with an increasing
559 rate of change of the magnetic field. Note, however, that a larger overall un-trapped percentage
560 does not necessarily lead to a larger ion percentage in the plasma sheet and magnetotail in Table
561 1, which does not include the percentage of ions reaching the magnetotail beyond $X_{GSM} < -66 R_E$.

Second, for a given overall percentage of un-trapped ions reaching the magnetosphere, the relative proportion between those reaching the plasma sheet and the magnetotail is expected to depend on the amplitude and polarity of the IMF, which control both the strength and the configuration of $\mathbf{E} \times \mathbf{B}$ convection. In particular, the increased strength of $\mathbf{E} \times \mathbf{B}$ convection under strongly southward IMF is expected to result in proportionally more of the un-trapped ions from the dayside reaching further down tail, and more of the un-trapped ions from the night side reaching lower L-shells. This in turn leads to a larger percentage of un-trapped ions reaching the magnetotail compared with the plasma sheet, since the fraction of un-trapped ions is larger on the dayside on average. This can be seen to be the case in Table 1 between storm C, in which B_Z was strongly southward for an extended duration before the onset and the plasma sheet to magnetotail ratio of un-trapped ions was about 0.56, and storm A, in which B_Z was northward or weakly southward and the corresponding ratio is 1.1.

Third, the solar wind dynamic pressure may also be an important factor in the plasma sheet to magnetotail ratio of the un-trapped ion percentage, depending on the prevailing IMF conditions (strength and polarity) and the resulting degree of coupling between the IMF and the Earth's internal field. This is because as P_{dyn} increases under southward IMF conditions, the magnetosphere becomes increasingly compressed and the magnitude of the convection electric field also increases [Shepherd and Ruohobiemi, 2000], resulting in larger centrifugal ion acceleration and stronger $\mathbf{E} \times \mathbf{B}$ convection, and ultimately a larger overall percentage of un-trapped ions reaching the magnetosphere and a larger magnetotail to plasma sheet percentage ratio; P_{dyn} is expected to be less of a factor under northward IMF conditions. Likewise, the rate at which P_{dyn} increases can also play a significant role, since a more rapid rise in P_{dyn} results in a

more rapid change in the magnetic field, which in turn leads to a larger increase in the overall percentage of un-trapped ions, as discussed above.

Fourth, the polarity of IMF B_Y is expected to affect the relative ratio of un-trapped ion percentage between the dawn and dusk magnetosphere, and the latter is expected to dominate on average. As shown previously in *Howarth and Yau* [2008], the ions preferentially feed the dusk sector of the plasma sheet when the IMF is duskward ($B_Y > 0$), and are more evenly distributed between the dusk and dawn sectors when the IMF is dawnward ($B_Y < 0$). Indeed, in Table 1, the dusk-to-dawn ratio of the percentage in the plasma sheet ranges from 1.5 to 4.9 and averages 2.7, while the corresponding ratio in the magnetotail ranges from 1.6 to 12.4 and averages 4.1. The ratio for the plasma sheet and magnetotail combined averages to 3.1, and varies from 1.7 in storm A, where B_Y was predominantly dawnward (negative), to 7.3 in storm E, where B_Y was predominantly and strongly duskward (B_Y as large as 28 nT) in the 2 hours immediately preceding the onset. In other words, the dusk-to-dawn ratio of the un-trapped ion percentage is generally higher when the IMF is duskward.

Finally, the overall level of geomagnetic activity, as characterized by the K_P index, is expected to affect both the overall percentage of trapped ions and the plasma sheet to magnetotail percentage ratio. As shown in Figure 1, the observed parallel ion velocity at the starting altitude is dependent on K_P ; in our simulation model, it is typically a factor of 1.5–2.0 higher under high- K_P conditions. This results in a larger percentage of ions gaining sufficient energy to overcome gravitation before reaching the turnaround altitude for a given level of centrifugal acceleration. At the same time, the larger initial parallel velocity also results in proportionally more of the un-trapped ions remaining at higher L-shells as they reach the magnetosphere for a given ion convection strength, and ultimately leads to a smaller plasma

607 sheet to magnetotail percentage ratio. It is clear that these five factors combine to affect the
608 overall distribution of un-trapped thermal-energy O^+ ions in the quiet-time period immediately
609 preceding a magnetic storm. However, because of the relatively small number of storms studied,
610 it is beyond the scope of this study to quantitatively delineate the relative importance of these
611 five factors.

4. Discussion and Summary

In Section 2 and 3 above, we extended the simulation model in *Howarth and Yau* [2008] to the case of time-dependent magnetic and convection electric field, to study the transport of thermal-energy polar wind O^+ ions in the quiet-time periods immediately preceding the main phase of five magnetic storms, when the IMF sometimes varies rapidly in polarity. Our study includes 2 large storms (minimum $Dst < -100$ nT) and 2 “super-storms” (minimum $Dst < -300$ nT), and storms in both the maximum and the declining phase of SC 23.

The simulation used the guiding-center equations of motion (equations 2 and 3) to solve for the single-particle trajectories of a number of ions starting from the high-altitude polar ionosphere during the 4-hr period preceding the onset of each storm, to determine the fraction (percentage) of ions that was able to overcome gravitation and reach the different regions of the magnetosphere as a result of centrifugal ion acceleration at higher altitudes. Every 10 minutes in the 4-hr period, the IGRF internal and Tsyganenko 1996 external magnetic field and the SuperDARN convection electric field models were updated, with a linear interpolation in between, and a total of 10,000 ions were “launched” from the starting altitude of 7000 km; a Monte Carlo technique was used to randomly select the initial position (invariant latitude and MLT) and velocity for each ion to ensure a statistically representative sampling of the ion phase space consistent with the observed polar wind ion velocity and temperature on Akebono [*Drakou et al.*, 1997; *Abe et al.*, 2004].

The result of our simulation is summarized as follows:

1. In the case of polar wind oxygen ions under typical quiet-time geomagnetic and solar wind conditions, the lowest-energy ions (≤ 2 eV) did not have sufficient energy to overcome gravitation before reaching the centrifugal acceleration altitude, but the higher-

energy ($> \sim 2$ eV) ions were able to do so and subsequently experience further acceleration and reach the magnetosphere at $\sim 10 R_E$ or beyond (Figure 3a): Ions originating at or near 75° invariant and 12 MLT experienced larger acceleration as they traversed regions of larger magnetic field curvature compared with those originating at higher invariant latitudes or other magnetic local times (Figure 3c).

2. A variable and small fraction (up to $\sim 24\text{--}36\%$) of the ions launched in the 4-hr period preceding a storm onset could overcome gravitation and become un-trapped and reach the plasma sheet and magnetotail (Figure 4 and 8, and Table 1); roughly a quarter of these ions is estimated to have reached the plasma sheet or magnetotail by the time of the storm onset, since their most probable and medium travel time was found to be about 3.4 and 3.8 hours, respectively (Figure 5).
3. On average, the dusk sector dominated the percentage of un-trapped ions in the plasma sheet and magnetotail. The ratio of un-trapped ions between the dawn and dusk magnetosphere was affected by the polarity of IMF B_Y , the dusk-to-dawn ratio of the percentage being in the range of 1.7 to 7.3 and 3.1 on average (Table 1 and Figure 8).
4. The averaged energy of the un-trapped O^+ ions increased with decreasing radial distance ($|X_{GSM}|$) in the magnetosphere, and the ions reached keV energy as they crossed the PSBL (Figure 6).
5. The distribution (percentage) of un-trapped ions that reached the plasma sheet and the magnetotail was strongly influenced by a number of factors. These included the IMF B_Y and B_Z components, the rate of change of the magnetic field, the solar wind dynamic pressure, and the level of geomagnetic activity as characterized by the K_p index (Table 1 and Figure 8).

6. An increase in IMF B_Y and B_Z resulted in an increase in the overall strength of $\underline{\mathbf{E}} \times \underline{\mathbf{B}}$ convection, particularly under southward IMF conditions, and led to larger centrifugal ion acceleration and ultimately a larger percentage of un-trapped ions.
7. An increased rate of change of the magnetic field also resulted in larger centrifugal acceleration, and for a given $\underline{\mathbf{E}} \times \underline{\mathbf{B}}$ convection strength led to a larger percentage of un-trapped ions.
8. An increase in convection strength and/or rate of magnetic field changes also resulted in an increase in the magnetotail to plasma sheet percentage ratio, due to more ions from the dayside becoming un-trapped compared with those from the night side on average for a given ion convection strength, and to more ions from the dayside and night side reaching higher and lower L-shells, respectively.
9. The effect of the solar wind dynamic pressure on the un-trapped ion percentage was dependent on the prevailing IMF strength and polarity, and was more pronounced under strongly southward IMF conditions.
10. Under high K_P conditions, the larger initial parallel ion velocity resulted in proportionally more of the un-trapped ions remaining at higher L-shells and ultimately a smaller plasma sheet to magnetotail percentage ratio.

As discussed in *Peterson et al.* [2009], the O^+ ion density in the plasma sheet is highly variable and dependent on magnetic activity level. Near solar minimum on ISEE-1 [*Lennartsson and Shelley*, 1986], the density of O^+ ions above 100 eV was found to range from ~ 0.01 at quiet times ($AE < 200$ nT) to $\sim 0.1 \text{ cm}^{-3}$ at active times ($AE \geq 200$ nT) between 10 and $22 R_E$, and to peak near $Y_{GSM} = 0$, particularly during active times. In addition, the density was found to exhibit a dawn-dusk asymmetry in favor the dusk sector, the quiet-time dusk-to-dawn density ratio being

about 2 in the $|Y_{GSM}| < 15 R_E$ region. Near solar maximum on Cluster [Kistler *et al.*, 2006], the measured O^+ density was $\sim 0.02 \text{ cm}^{-3}$ at $19 R_E$ in quiet intervals before substorms. The large asymmetry (factor of 1.5 to ~ 5 dusk-to-dawn ratio) in O^+ plasma sheet ion density in Figure 8 and Table 1 is clearly in good qualitative accord with the ISEE-1 data at least insofar as dawn-dusk asymmetry, assuming that the observed asymmetry in the ISEE-1 data near solar minimum was not strongly dependent on solar activity level.

On the question of low-energy plasma sheet O^+ ions, the low-energy cut-off of the ISEE-1 ion mass spectrometer (100 eV/e) precluded its detection of O^+ ions below 100 eV, whose presence in the plasma sheet is possible, for example at times of low $E \times B$ velocities. On Geotail, non-mass-resolved cold ions below 100 eV were frequently observed at comparable densities to the hot ions in the eclipsed regions of the central plasma sheet [Seki *et al.*, 2003]. On Cluster, most of the O^+ ions that were measured with the ion composition and distribution function (CODIF) instrument, which had a 40-eV low-energy cut-off, were above 100 eV [Kistler *et al.*, 2005]. Figure 8 suggests that in the absence of other additional acceleration processes, a large fraction of the un-trapped O^+ ions reaching the plasma sheet typically had energies of 100 eV or greater (color-coded in red or orange in Figure 6) due to centrifugal ion acceleration; this appears to be consistent with the Cluster results.

Using Cluster magnetic field and CODIF ion composition data, Nilsson *et al.* [2008] investigated the role of centrifugal ion acceleration in the altitude range of $5 - 12 R_E$, by comparing the accumulated effect of the acceleration over this altitude range with the observed parallel O^+ ion velocity in each of several orbits. It was found that a large fraction of the observed ion velocity may be attributed to the acceleration, and that the observed velocity was consistent with initial ion energy of about 40 eV (velocity of about 20 km/s) at $5 R_E$ under

realistic ion convection conditions in a steady-state magnetic field. Due to spacecraft charging and other technical reasons, the analysis in *Nilsson et al.* [2008] was confined to ion data above 40 eV and focused on acceleration events of higher-energy ions on auroral field lines; it excluded lower-energy ions such as the polar wind whose energy-per-charge was below the spacecraft potential, which was typically in the range of 5–40 V in the polar cap [*Eriksson et al.*, 2006]. In comparison, the two polar wind O⁺ ions in Figure 3b above had lower energies (<5 and <10 eV, respectively) by the time they reached 5 R_E. The larger “initial” ion energy on Cluster may be attributed to the dominance of higher-energy ions such as the cleft ion fountain and upwelling ions in the Cluster analysis, which have higher energies than polar wind ions but are not always observationally separable from the polar wind ions, as noted in the Introduction section.

In equation 2 and 4 above, each of the three acceleration terms can in principle give rise to ion acceleration or deceleration in a given instance depending on the relative orientation between the magnetic and convection electric fields and their spatial or temporal gradients. Statistically, ion acceleration due to the parallel and perpendicular terms was observed to be much more frequent compared with ion deceleration on Cluster: the acceleration-to-deceleration occurrence frequency ratio being 2–10 [*Nilsson et al.*, 2008]; the dominance of acceleration over deceleration is not surprising given the topology of the magnetic field at high altitudes. In contrast, the occurrence frequency ratio of ion acceleration due to the temporal term was near unity. On average, the magnitude of ion acceleration due to the parallel and perpendicular terms was about 5 and 3 m s⁻², respectively, and larger compared with the temporal term (<2 m s⁻²) [*Nilsson et al.*, 2008]. This implies that in the case of a time-dependent magnetic field, the parallel and perpendicular terms are expected to dominate the overall effect of centrifugal acceleration, and explains the modest range of un-trapped ion percentage (24–36%) in Table 1

for the 5 storms, which correspond to different time-dependent magnetic and convection electric field conditions.

The estimated volume of the quiet-time plasma sheet is about $4 \times 10^{24} \text{ m}^3$ [Chappell *et al.*, 1987]. As noted above, the observed quiet-time O^+ density in the plasma sheet on ISEE-1 was about 0.01 cm^{-3} near solar minimum [Lennartsson and Shelley, 1986], and increased by a factor of 3 between early 1978 and early 1979 in the early ascending phase of the solar cycle, when the solar rotation-averaged $F_{10.7}$ solar radio flux index increased from ~ 100 to ~ 200 . The ISEE-1 observation suggests a quiet-time plasma sheet O^+ density of $>0.03 \text{ cm}^{-3}$ near solar maximum. In other words, the O^+ mass content in the plasma sheet is estimated to be ~ 260 and $>780 \text{ kg}$ near solar minimum and maximum, respectively.

Like its plasma sheet counterpart, the O^+ ion density in the ring current is also highly dynamic. After all, as Korth *et al.* [2000] showed using CRRES data, the ring current O^+ ions are believed to come from the plasma sheet and not directly from the ionosphere, including low-energy ions below 30 keV in the main phase of a storm. Most known mechanisms for transporting plasma sheet ions to the ring current and energizing them to ring current energies are believed to be mass independent [Li *et al.*, 2003]. However, observational evidence suggestive of mass-dependent transport or energization processes does exist, for example on Polar [Pulkkinen *et al.*, 2001]. Using AMPTE/CHEM data, Daglis *et al.* [1993] reported an O^+/H^+ energy density ratio of ~ 0.06 in 1–300 keV ring current ions at very quiet times ($\text{AE} < 30 \text{ nT}$) near solar minimum. Based on the energetic upflowing ion observation of Yau *et al.* [1988] on DE-1, and the plasma sheet observation of Lennartsson and Shelley [1986] on ISEE-1, as noted above, the corresponding O^+/H^+ energy density ratio near solar maximum may be expected to be larger by a factor of ~ 3 or more.

Greenspan and Hamilton [2000] used AMPTE data to test the Dessler-Parker-Sckopke (DPS) relation [*Sckopke*, 1966], and showed the ratio of total ring current energy to the magnitude of Dst to be approximately 2×10^{29} keV/nT. Using a value of -25 nT for quiet-time Dst, and a quiet-time O^+/H^+ ring current density ratio of 0.06 near solar minimum and 0.3 near solar maximum by assuming O^+ and H^+ to have comparable energy spectra, the estimated O^+ mass content in the ring current is estimated to be ~ 150 kg near solar minimum and ~ 590 kg near solar maximum. In comparison, the corresponding estimates in *Peterson et al.* [2009] were 50 and 300 kg. The factor-of-3 difference between the two sets of estimates may be attributed to the factor-of-2 larger Dst and factor-of-6 smaller O^+/H^+ density ratio values used in *Peterson et al.* [2009].

In comparison, as discussed in the Introduction section, the density of O^+ polar wind is seasonally dependent and is on the order of a few to ~ 30 cm^{-3} near solar maximum. Assuming an seasonally averaged density of 10 cm^{-3} , a K_P -averaged parallel ion velocity of 3 km/s, and an averaged un-trapped ion percentage of 25% reaching the plasma sheet (from Table 1), the flux of un-trapped O^+ ions reaching the plasma sheet is $\sim 7.5 \times 10^5$ $\text{cm}^{-2} \text{ s}^{-1}$. Using the dipole approximation, the flux tube area over an invariant latitude range in both hemispheres is given by [*Yau et al.*, 1988]

$$A = 4\pi R_r^2 \left\{ \left[1 - (R_r / R_E) \cos^2 \Lambda_2 \right]^{1/2} - \left[1 - (R_r / R_E) \cos^2 \Lambda_1 \right]^{1/2} \right\} \quad (5)$$

where R_r is the geocentric distance, R_E is the Earth radius, and Λ_1 and Λ_2 are the lower and upper limits of invariant latitude, respectively. Assuming uniform polar wind poleward of 70° invariant, the total area of polar-wind flux tubes at 7000 km altitude in both hemispheres is 2.95×10^{18} cm^2 , and this corresponds to a total rate of un-trapped $\sim 2.2 \times 10^{24}$ O^+ ions s^{-1} and a

772 mass injection rate of ~ 200 kg/hr into the plasma sheet. For an estimated O^+ plasma sheet mass
773 content of ~ 780 kg, this suggests a filling time of ~ 4 hrs.

774 In summary the simulations and analysis presented show that centrifugal acceleration at
775 higher altitudes (above $\sim 3 R_E$ altitude) energizes a significant fraction of thermal O^+ to escape
776 velocity and that the fraction of this population reaching the plasma sheet is a factor of ~ 3 larger
777 in the dusk sector on average compared with the dawn sector. Our results are consistent with the
778 picture that low-energy ion flow constitutes a significant “in-transit” oxygen ion population over
779 a period of a few (~ 4) hours preceding a magnetic storm, which explains the presence of O^+ ions
780 in the ring current shortly after the onset of the main phase of the storm, when the heavy ions
781 could potentially modify the evolution of the ring current.

782

783 Acknowledgement

784 The authors gratefully acknowledge the support of the Canadian Space Agency and the Natural
785 Science and Engineering Research Council (NSERC) Industrial Research Chair Program for this
786 research. W.K.P. was supported by NASA Grant NNX12AD25G.

References

- Abe, T., A.W. Yau, S. Watanabe, M. Yamada, and E. Sagawa (2004), Long-term variation of the polar wind velocity and its implication for the ion acceleration process: Akebono/suprathermal ion mass spectrometer observations, *J. Geophys. Res.*, *109*, 10.1029/2003JA010223, 2004
- Chappell, C. R., T. E. Moore, and J. H. Waite Jr. (1987), The ionosphere as a fully adequate source of plasma for the Earth's magnetosphere, *J. Geophys. Res.*, *92*(A6), 5896–5910
- Cladis, J.B., Parallel acceleration and transport of ions from the polar ionosphere to the plasmasheet, *Geophys. Res. Lett.* *13*, 893-896, 1986.
- Cully, C. M., E.F. Donovan, A.W. Yau, and G.G. Arkos (2003), Akebono suprathermal mass Spectrometer observations of low-energy ion outflow: dependence on magnetic activity and solar wind conditions, *J. Geophys. Res.*, *108*, 1093, doi:10.1029/2001JA009200, 2003
- Cully, C. M., E.F. Donovan, A.W. Yau, and H.J. Opgenoorth, Supply of thermal ionospheric ions to the central plasma sheet, *J. Geophys. Res.*, *108*, 1092, doi:10.1029/2002JA009457, 2003b.
- Daglis, I.A., E.T. Sarris, and B. Wilken, (1993) AMPTE/CCE CHEM observations of the energetic ion population at geosynchronous altitudes, *Ann. Geophys.*, *11*, 685– 696
- Delcourt, D.C., C.R. Chappell, T.E. Moore, and J.H. Waite Jr. (1989), A three dimensional numerical model of ionospheric plasma in the magnetosphere, *J. Geophys. Res.*, *94*, 11893–11920
- Delcourt, D.C., J.A. Sauvaud, and T.E. Moore, (1993), Polar wind ion dynamics in the magnetotail, *J. Geophys. Res.*, *98*, 9155–9169

809 Delcourt, D.C., T.E. Moore, and C.R. Chappell, (1994), Contribution of low-energy ionospheric
810 protons to the plasma sheet, *J. Geophys. Res.*, *99*, 5681–5689

811 Drakou, E., A.W. Yau, and T. Abe (1997), Ion temperature measurements from the Akebono
812 suprathermal mass spectrometer: Application to the polar wind, *J. Geophys. Res.*, *102*, 17523–
813 17539

814 Ebihara, Y., M. Yamada, S. Watanabe, and M. Ejiri (2006), Fate of outflowing suprathermal
815 oxygen ions that originate in the polar ionosphere, *J. Geophys. Res.*, *111*, A04219,
816 doi:10.1029/2005JA011403

817 Eriksson, A.I., M. Andre, B. Klecker, H. Laakso, P.A. Lindqvist, F. Mozer, G. Paschmann, A.
818 Pedersen, J. Quinn, R. Torbert, K. Torkar, and H. Vaith (2006), Electric field measurements
819 on Cluster: comparing double-probe and electron drift techniques, *Ann. Geophys.*, *24*, 275–
820 289

821 Finlay, C.C., S. Maus, C. Beggan, et al. (2010), International Geomagnetic Reference Field: the
822 eleventh generation, *Geophys. J. Int.*, *183*, 1216-1230, doi: 10.1111/j.1365-
823 246X.2010.04804.x

824 Fok, M.C., R.A. Wolf, R.W. Spiro, and T. E. Moore, Comprehensive computational model of
825 Earth's ring current, *J. Geophys. Res.*, *106*, 8417-8424, 2001

826 Greenspan, M.E., and D.C. Hamilton (2000), A test of the Dessler-Parker-Sckopke relation
827 during magnetic storms, *J. Geophys. Res.* *105*, 5419-5430

828 Howarth, A., and A.W. Yau (2008), The effects of IMF and convection on thermal ion outflow
829 in magnetosphere-ionosphere coupling, *J. Atmos. Solar Terr. Phys.*,
830 doi:10.1016/j.jastp.2008.08.008

831 Huddleston, M. M., C.R. Chappell, D.C. Delcourt, T.E. Moore, B.L. Giles, and M.O. Chandler
 832 (2005), An examination of the process and magnitude of ionospheric plasma supply to the
 833 magnetosphere, *J. Geophys. Res.*, *110*, A12202, doi:10.1029/2004JA010401
 834 Hultqvist, B., M. Øieroset, G. Passman, and R. Treuman, Editors (1999), *Magnetospheric*
 835 *Plasma Sources and Losses*, Kluwer Academic Publishers, Dordrecht, Boston, London
 836 Jordanova, Vania K., New insights on geomagnetic storms from model simulations using multi-
 837 spacecraft data, *Space Science Rev.* *107*, 157, 2003.
 838 Kistler, L. M., et al. (2005), Contribution of nonadiabatic ions to the cross-tail current in an O⁺
 839 dominated thin current sheet, *J. Geophys. Res.*, *110*, A06213, doi:10.1029/2004JA010653
 840 Kistler, L. M., et al. (2006), Ion composition and pressure changes in storm time and nonstorm
 841 substorms in the vicinity of the near-Earth neutral line, *J. Geophys. Res.*, *111*, A11222,
 842 doi:10.1029/2006JA011939
 843 Kitamura, N., A. Shinbori, Y. Nishimura, T. Ono, M. Iizima, and A. Kumamoto (2009),
 844 Seasonal variations of the electron density distribution in the polar region during
 845 geomagnetically quiet periods near solar maximum, *J. Geophys. Res.*, *114*, A01206,
 846 doi:10.1029/2008JA013288
 847 Kitamura, N., Y. Nishimura, T. Ono, Y. Ebihara, N. Terada, A. Shinbori, A. Kumamoto, T. Abe,
 848 M. Yamada, S. Watanabe, A. Matsuoka, and A.W. Yau (2010), Observations of very-low-
 849 energy (<10 eV) ion outflows dominated by O⁺ ions in the region of enhanced electron
 850 density in the polar cap magnetosphere during geomagnetic storms, *J. Geophys. Res.*, *115*,
 851 A00J06, 12 pp., 2010 doi:10.1029/2010JA015601

852 Korth, A., R.H.W. Friedel, C.G. Mouikis, J.F. Fennell, J.R. Wygant, and H. Korth (2000),
853 Comprehensive particle and field observations of magnetic storms at different local times
854 from the CRRES spacecraft, *J. Geophys. Res.*, *105*, 18729-18740

855 Lennartsson, W., and E.G. Shelley (1986), Survey of 0.1- to 16-keV/e plasma sheet ion
856 composition, *J. Geophys. Res.*, *91*(A3), 3061–3076.

857 Lennartsson, O.W., H.L. Collin, and W.K. Peterson (2004), Solar wind control of Earth's H^+ and
858 O^+ outflow rates in the 15-eV to 33-keV energy range, *J. Geophys. Res.*, *109*, A12212,
859 doi:10.1029/2004JA010690

860 Li, X.L., I. Roth, M. Temerin, J.R. Wygant, M.K. Hudson, and J.B. Blake (1993), Simulation of
861 the prompt energization and transport of radiation belt particles during the March 24, 1991
862 SSC, *Geophys. Res. Lett.* *20*, 2423-2426

863 Nilsson, H., M. Waara, O. Marghitu, et al. (2008), An assessment of the role of the centrifugal
864 acceleration mechanism in high altitude polar cap oxygen ion outflow, *Ann. Geophys.* *26*,
865 145-157

866 Northrop, T.G. (1963), *The Adiabatic Motion of Charged Particles*, Wiley-Interscience, New
867 York

868 Peterson, W.K., L. Andersson, B.C. Callahan, H.L. Collin, J.D. Scudder, and A.W. Yau (2008),
869 Solar-minimum quiet time ion energization and outflow in dynamic boundary related
870 coordinates, *J. Geophys. Res.*, *113*, A07222, doi:10.1029/2008JA013059

871 Peterson, W.K., L. Andersson, B. Callahan, S.R. Elkington, R.W. Winglee, J.D. Scudder, and
872 H.L. Collin (2009), Geomagnetic activity dependence of O^+ in transit from the ionosphere, *J.*
873 *Atmos. Solar Terr. Phys.*, *71*, 1623-1629

874 Pulkkinen, T.I., et al. (2001), Ring current ion composition during solar minimum and rising
875 solar activity: Polar/Cammice/MICS results, *J. Geophys. Res.*, *106*, 19131-19147
876 doi:10.1029/2000JA003036

877 Ruohoniemi, J.M., and R.A. Greenwald (1996), Statistical patterns of high-latitude convection
878 obtained from Goose Bay HF radar observations, *J. Geophys. Res.*, *101*, 21743–21763

879 Sckopke, N. (1966), A general relation between the energy of trapped particles and the
880 disturbance field near the Earth, *J. Geophys. Res.*, *71*, 3125-3130

881 Seki, K., et al. (2003), Cold ions in the hot plasma sheet of Earth's magnetotail, *Nature*, *422*,
882 589-592

883 Shepherd, S.G., and J.M. Ruohoniemi (2000), Electrostatic potential patterns in the high-latitude
884 ionosphere constrained by SuperDARN measurements, *J. Geophys. Res.*, *105*, 23005–23014

885 Su, Y.J., J.L. Horwitz, T.E. Moore, B.L. Giles, M.O. Chandler, P.D. Craven, M. Hirahara, and
886 C.J. Pollock (1998), Polar wind survey with the thermal ion dynamics experiment/plasma
887 source instrument suite aboard POLAR, *J. Geophys. Res.*, *103*, 29305–29337

888 Sugiura, M., and D.J. Poros, Hourly values of equatorial Dst for years 1957 to 1970, Rep. X-645-
889 71-278, Goddard Space Flight Center, Greenbelt, Maryland, 1971.

890 Tsyganenko, N.A. (1989), A magnetospheric magnetic field model with a warped tail current
891 sheet, *Planet. Space Sci.*, *37*, 5–20.

892 Tsyganenko, N.A. (1995), Modeling the Earth's magnetospheric magnetic field confined within
893 a realistic magnetopause, *J. Geophys. Res.*, *100*, 5599–5612

894 Tsyganenko, N.A., and D.P. Stern (1996), Modeling the global magnetic field of the large-scale
895 Birkeland current systems, *J. Geophys. Res.*, *101*, 27187-27198 doi:10.1029/96JA02735

896 Weimer, D. R. (2001), An improved model of ionospheric electric potentials including substorm
 897 perturbations and application to the Geospace Environment Modeling November 24, 1996,
 898 event, *J. Geophys. Res.*, *106*, 407-416
 899 Yau, A.W., and M. Andre (1997), Source processes in the high latitude ionosphere, *Space Sci. Rev.*,
 900 *80*, 1-25
 901 Yau, A.W., E.G. Shelley, W.K. Peterson, and L. Lenchyshyn (1985), Energetic auroral and polar
 902 ion outflow at DE-1 altitudes: magnitude, composition, magnetic activity dependence, and long-
 903 term variations. *J. Geophys. Res.* *90*, 8417-8432
 904 Yau, A.W., W.K. Peterson, and E.G. Shelley(1988), Quantitative parameterization of energetic
 905 ionospheric ion outflow, in *Modeling Magnetospheric Plasma, Geophysical Monograph 44*,
 906 American Geophysical Union, Washington, DC. pp. 211-217
 907 Yau, A.W., B.A. Whalen, and E. Sagawa (1991), Minor ion composition in the polar ionosphere,
 908 *Geophys. Res. Lett.* *18*, 345-348
 909 Yau, A.W., T. Abe, and W.K. Peterson (2007), The polar wind: recent observations, *J. Atmos.*
 910 *Solar Terr. Phys.*, *69*, 1936-1983
 911 Zaharia, S., V. K. Jordanova, M. F. Thomsen, and G. D. Reeves (2006), Self-consistent modeling
 912 of magnetic fields and plasmas in the inner magnetosphere: Application to a geomagnetic
 913 storm, *J. Geophys. Res.*, *111*, A11S14, doi:10.1029/2006JA011619.

914 Table 1 Solar wind pressure, IMF, and simulated thermal O⁺ ion percentage in magnetic storms

Event ID & Date	Onset time (UT)	min Dst (nT)	Time of P_{dyn} inc (UT)	max P_{dyn} (nP)	After onset		Before onset		Averaged percentage (range) of un-trapped ions launched before onset				
					B_Z (nT)	B_Y (nT)	B_Z (nT)	B_Y (nT)	Plasma sheet		Tail		Total
									Dusk	Dawn	Dusk	Dawn	
A 2000/04/06	1645	-320	1645	12	-30 to -10	-20 to 10	-5 to 5	-2 to -8	10.9 (7-16)	5.9 (3-8)	9.8 (4-16)	5.8 (2-9)	32.4 (24-38)
B 2000/11/06	1340	-175	1430	5	-12 to 9	0 to 10	-10 to 10	-10 to 10	16.2 (11-23)	4.8 (4-6)	9.8 (5-14)	5.5 (3-9)	36.4 (34-39)
C 2001/11/06	0200	-300	N/A	N/A	N/A	N/A	-12 to -5	15 to 20	5.1 (4-6)	3.5 (2-4)	11.4 (10-14)	3.9 (2-6)	23.9 (20-27)
D 2003/05/29	1700	-80	1610	17	-32 to 30	-22 to 28	-10 to 10	-10 to 10	9.0 (6-11)	4.5 (2-6)	9.8 (5-14)	6.2 (2-10)	29.6 (24-33)
	2140	-100	≤2125	≤50	-26 to 20	-12 to 20							
	2230	-170	2240	46	-16 to 17								
E 2005/01/21	1940	-100	1850	85	-2 to 22	-12 to 22	-25 to 30	-30 to 28	12.2 (8-15)	2.5 (1-4)	14.9 (8-19)	1.2 (0-5)	30.8 (25-33)

915

Figure Captions

Figure 1 Averaged polar wind O^+ velocity between 6000 and 8000 km altitude observed on Akebono near solar maximum, for low and high K_p conditions; left: $K_p \leq 2$; right: $K_p > 2$; adapted from *Abe et al.* [2004]

Figure 2 Geomagnetic and solar wind conditions preceding and during the 6 April 2000 magnetic storm: from top to bottom: K_p , SYM-H, solar wind dynamic pressure, and IMF B_Y and B_Z components

Figure 3a Examples of simulated trajectories of polar wind O^+ ions originating at 7000 km altitude, 75° invariant and 12 MLT in the storm of 6 April 2000

Figure 3b Ion energy of polar wind O^+ ions originating at 7000 km altitude, 75° invariant and 12 MLT, and starting at 2- and 3-eV, respectively, along their respective trajectories in the adiabatic region

Figure 3c Simulated trajectories of 2-eV polar wind O^+ ions originating from different invariant latitude and MLT locations at 7000 km altitude

Figure 4 Distribution of simulated ion destinations in terms of the percentage of ions at each destination (region of the magnetosphere) as a function of the launch time of the ions before and during the 6 April 2000 magnetic storm: the dayside (brown), magnetopause (green), distant tail ($X < -66 R_E$; light blue), dawn and dusk tail (red and gold), dawn and dusk plasma sheet (purple and dark blue), and total non-trapped (black)

Figure 5 Number of ions arriving at each magnetospheric destination as a function of their arrival time before and during the 6 April 2000 magnetic storm, using the same color codes for the different regions of the magnetosphere as in Figure 4 except for the black trace, which denotes the number of trapped ions

Figure 6 Distribution of about 148,000 simulated O^+ ions that reached the plasma sheet or the magnetotail in the magnetic storm of 6 April 2000

Figure 7 (a) the 3-hr K_P index; (b) 1-min SYM-H; and time-shifted (from ACE) (c) solar wind dynamic pressure, P_{dyn} , (d) IMF B_Y and (e) B_Z , preceding and during five magnetic storms on (A) 6 April 2000 (black), (B) 6 November 2000 (blue), (C) 5 November 2001 (green), (D) 29 May 2003 (brown), and (E) 21 January 2005 (red), respectively

Figure 8 Percentage of un-trapped thermal-energy O^+ ions reaching the dusk (solid circles) and dawn (no circles) sectors of the (a) plasma sheet and (b) magnetotail, as a function of the launch time of the ions, 0–4 hrs before the onset of the main phase of the magnetic storms on (A) 6 April 2000 (black), (B) 6 November 2000 (blue), (C) 5 November 2001 (green), (D) 29 May 2003 (brown), and (E) 21 January 2005 (red), respectively; and 2–6 hrs before the onset on (C) 5 November 2011 with the data display shifted to the right by 2 hours in the figure.

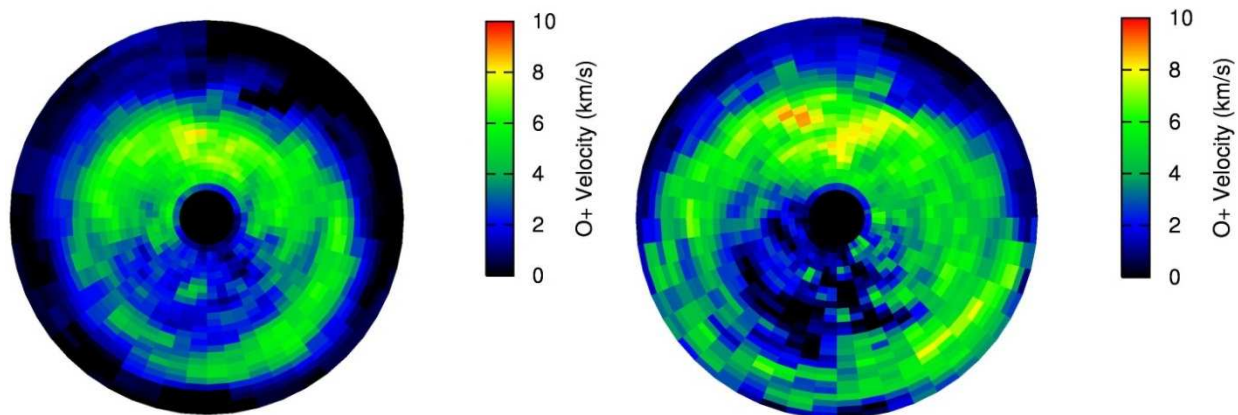
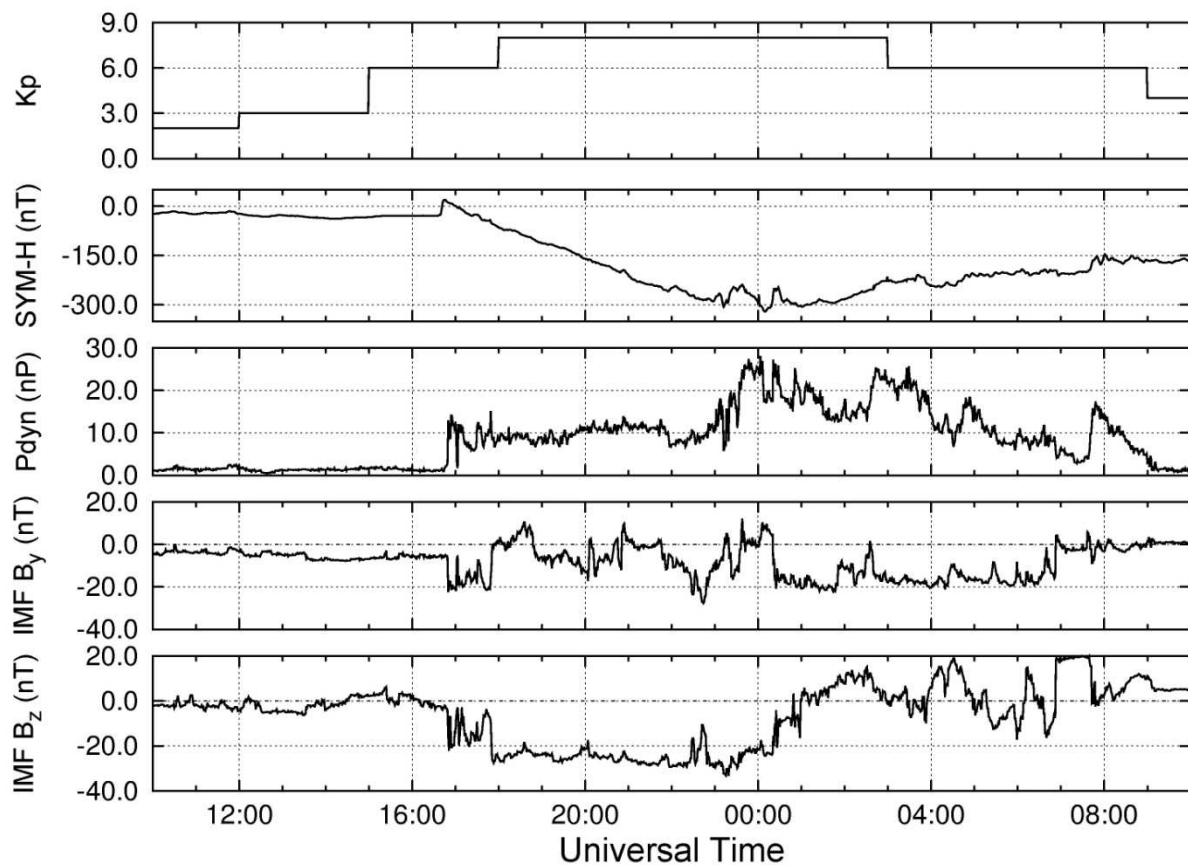


Figure 1 Averaged polar wind O⁺ velocity between 6000 and 8000 km altitude observed on Akebono near solar maximum, for low and high K_p conditions; left: K_p ≤ 2; right: K_p > 2; adapted from *Abe et al.* [2004]



970

971

972 Figure 2 Geomagnetic and solar wind conditions preceding and during the 6 April 2000 magnetic
 973 storm: from top to bottom: K_p , SYM-H, solar wind dynamic pressure, and IMF B_y and B_z
 974 components

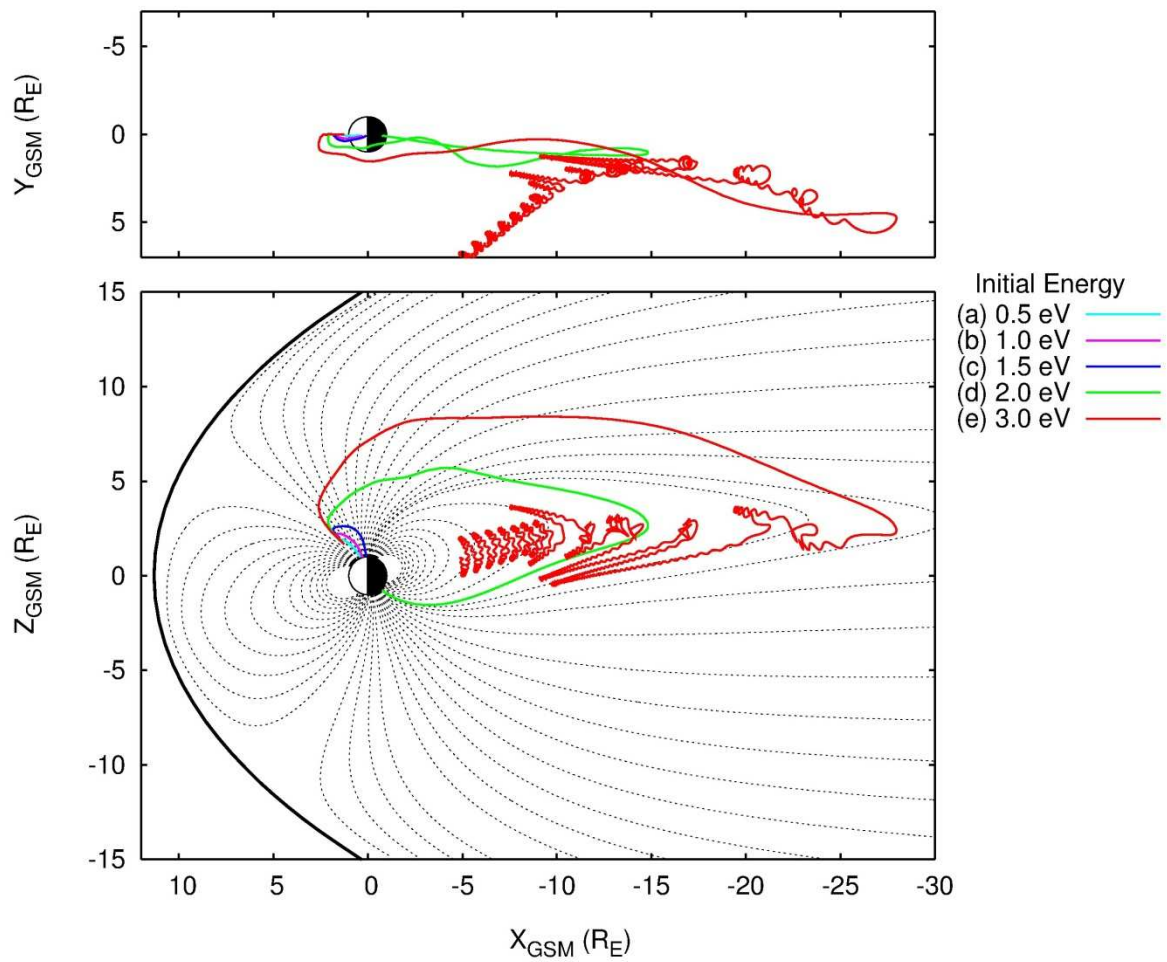


Figure 3a Examples of simulated trajectories of polar wind O^+ ions originating at 7000 km altitude, 75° invariant and 12 MLT in the storm of 6 April 2000

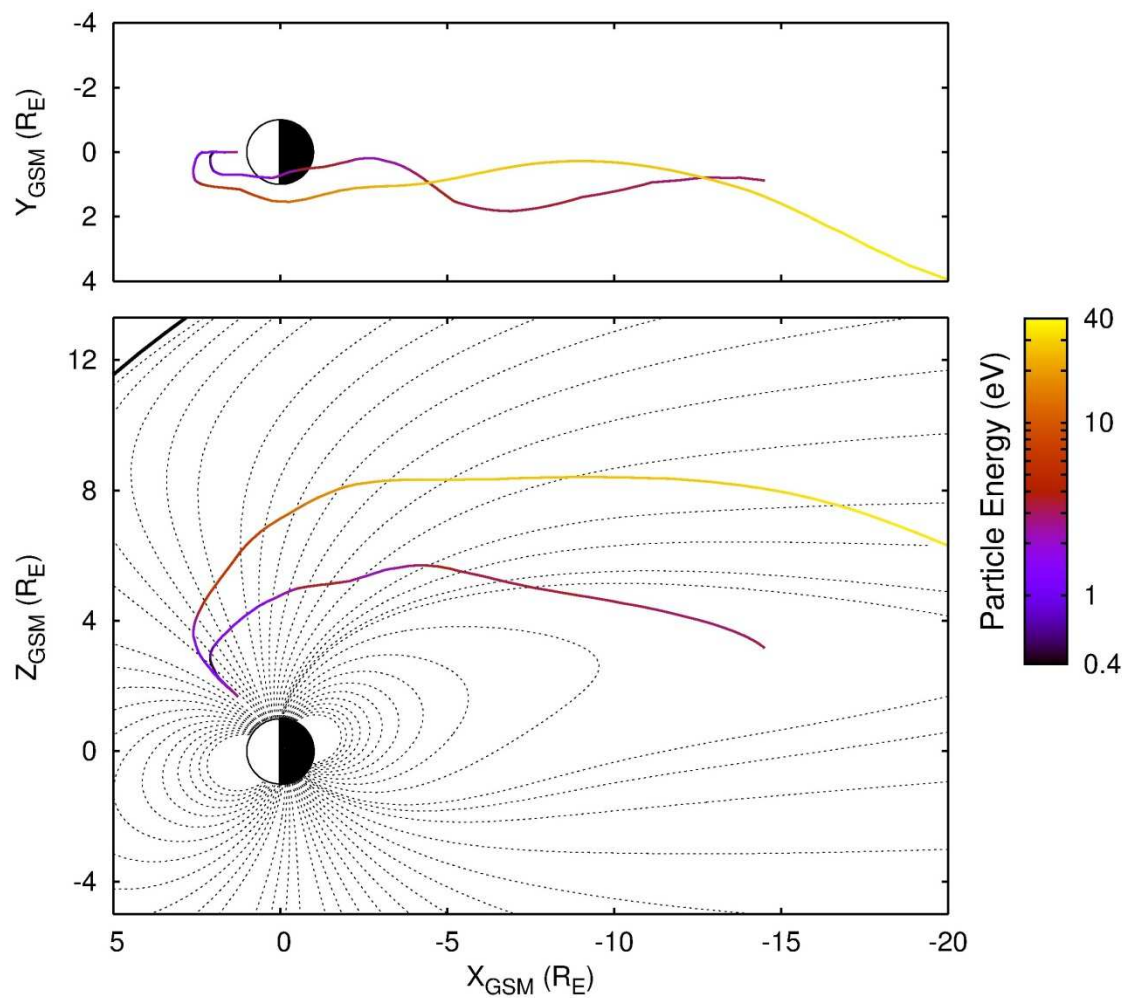
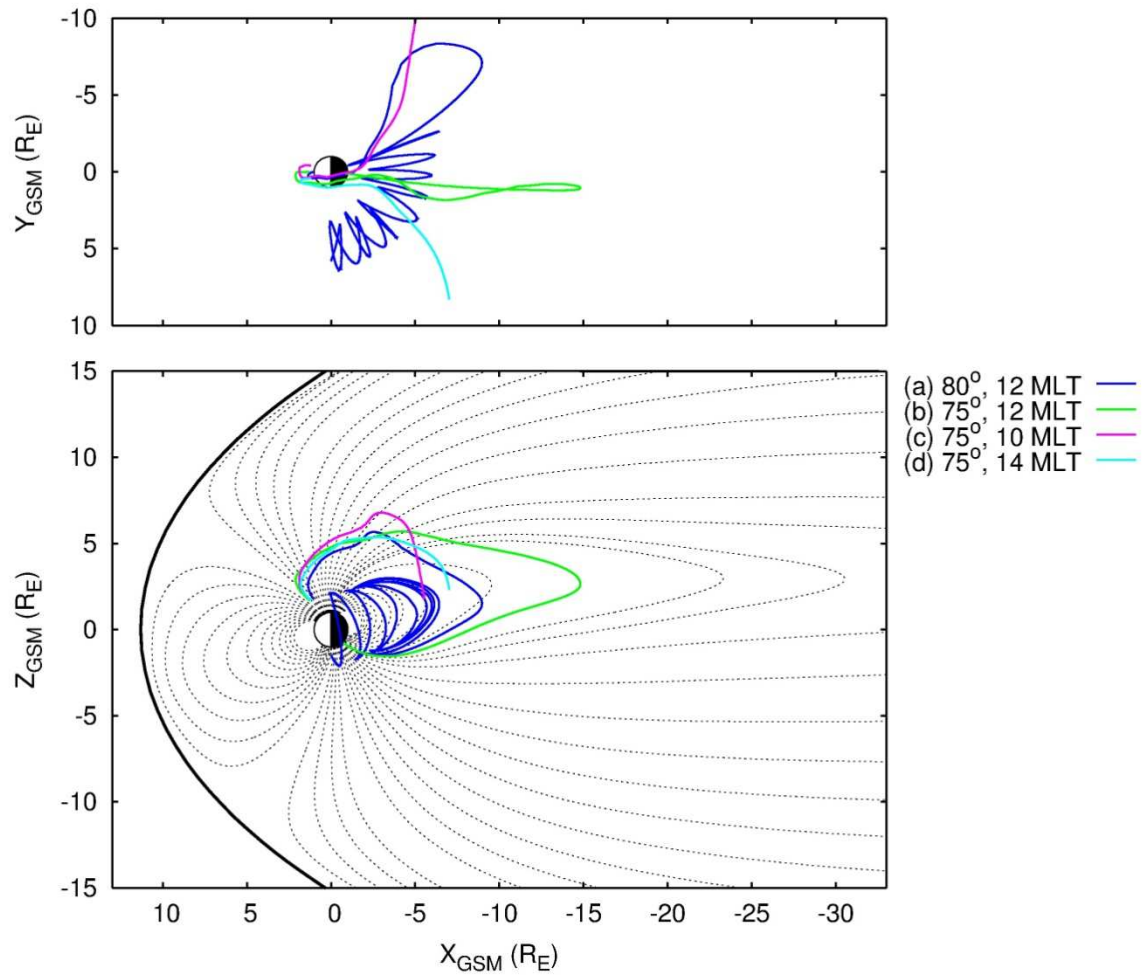


Figure 3b Ion energy of polar wind O^+ ions originating at 7000 km altitude, 75° invariant and 12 MLT, and starting at 2- and 3-eV, respectively, along their respective trajectories in the adiabatic region

986



987

988 Figure 3c Simulated trajectories of 2-eV polar wind O^+ ions originating from different invariant
 989 latitude and MLT locations at 7000 km altitude

990

991

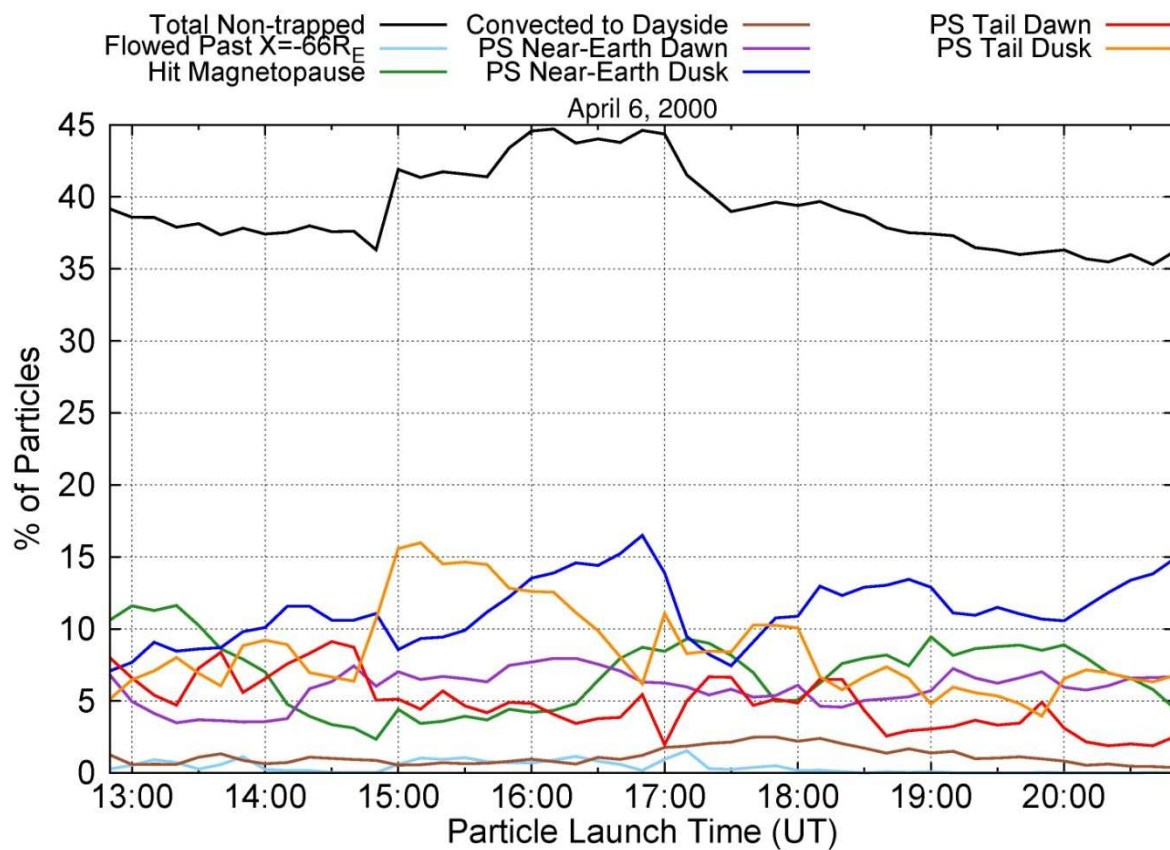


Figure 4 Distribution of simulated ion destinations in terms of the percentage of ions at each destination (region of the magnetosphere) as a function of the launch time of the ions before and during the 6 April 2000 magnetic storm: the dayside (brown), magnetopause (green), distant tail ($X < -66 R_E$; light blue), dawn and dusk tail (red and gold), dawn and dusk plasma sheet (purple and dark blue), and total non-trapped (black)

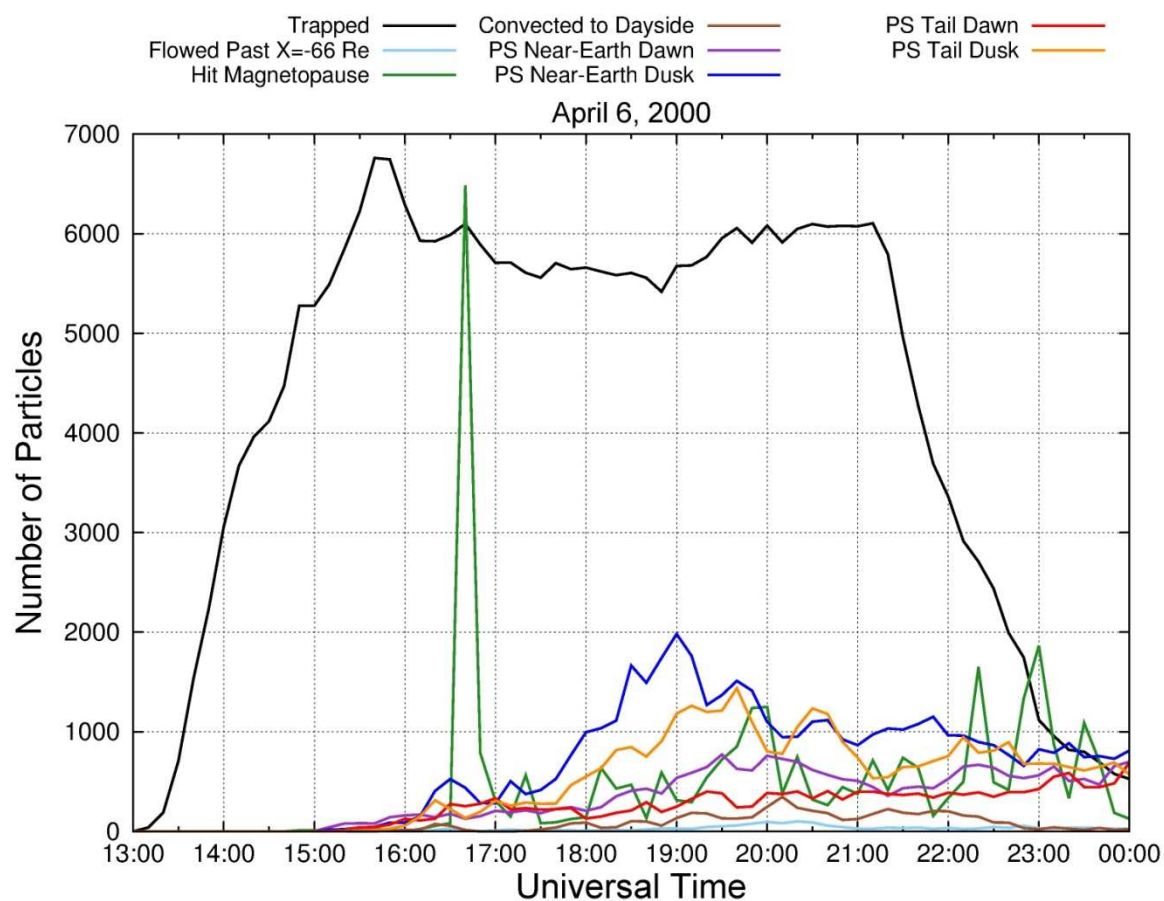


Figure 5 Number of ions arriving at each magnetospheric destination as a function of their arrival time before and during the 6 April 2000 magnetic storm, using the same color codes for the different regions of the magnetosphere as in Figure 4 except for the black trace, which denotes the number of trapped ions

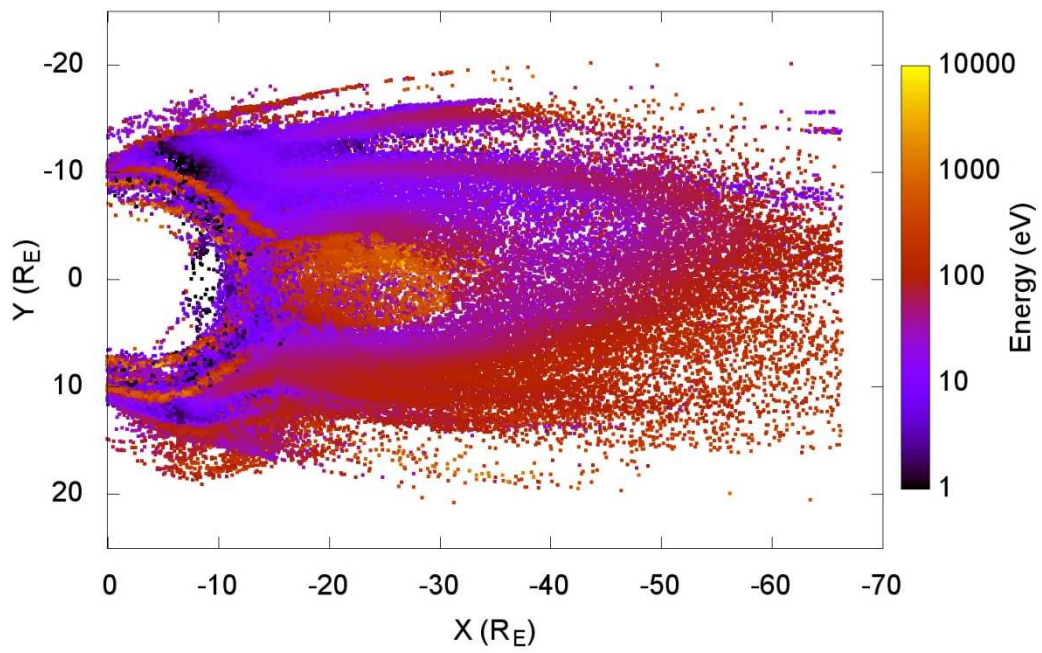


Figure 6 Distribution of about 148,000 simulated O^+ ions that reached the plasma sheet or the magnetotail in the magnetic storm of 6 April 2000

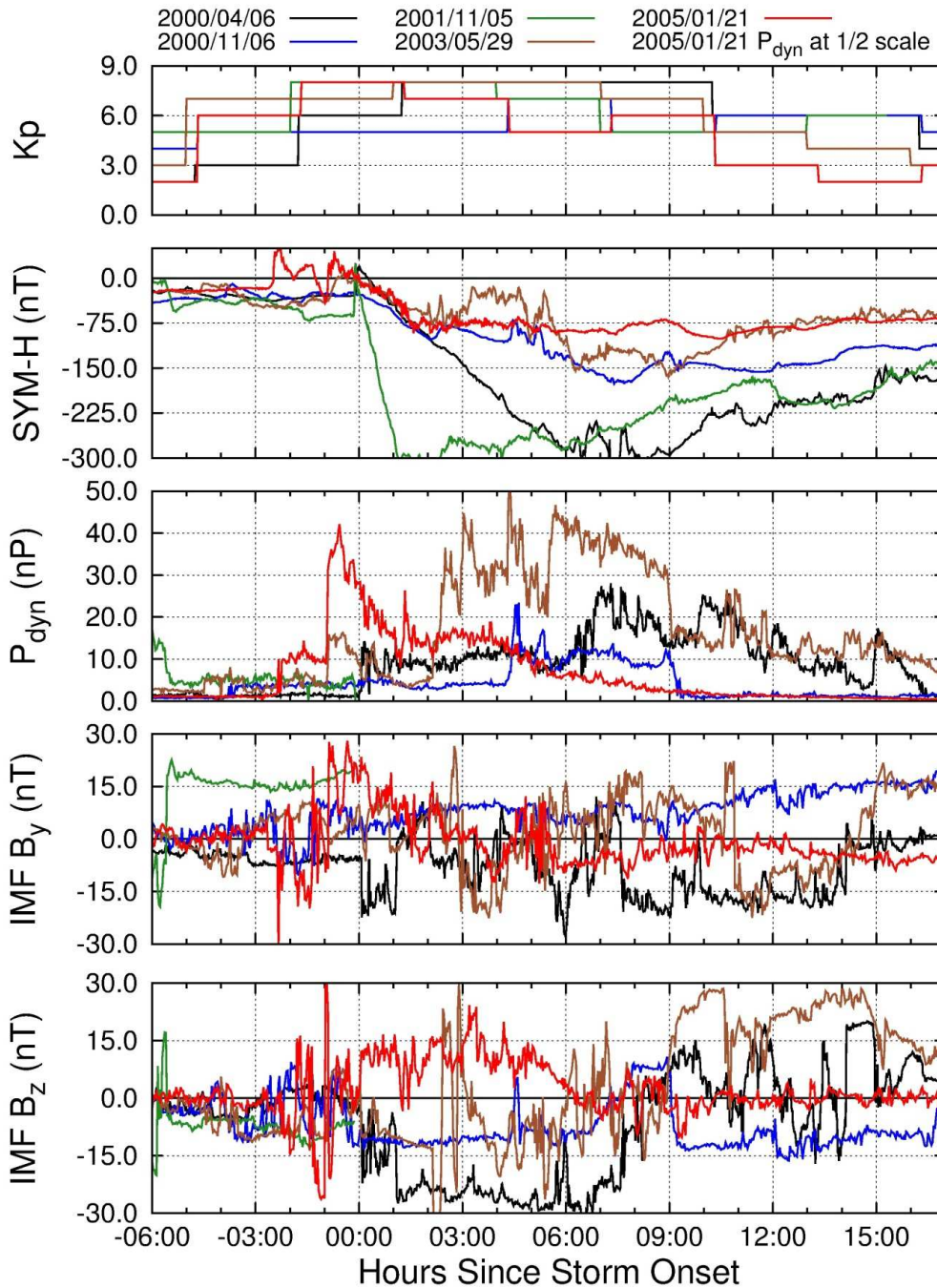


Figure 7 (a) the 3-hr K_p index; (b) 1-min $SYM-H$; and time-shifted (from ACE) (c) solar wind dynamic pressure, P_{dyn} , (d) $IMF B_y$ and (e) B_z , preceding and during five magnetic storms on (A) 6 April 2000 (black), (B) 6 November 2000 (blue), (C) 5 November 2001 (green), (D) 29 May 2003 (brown), and (E) 21 January 2005 (red), respectively

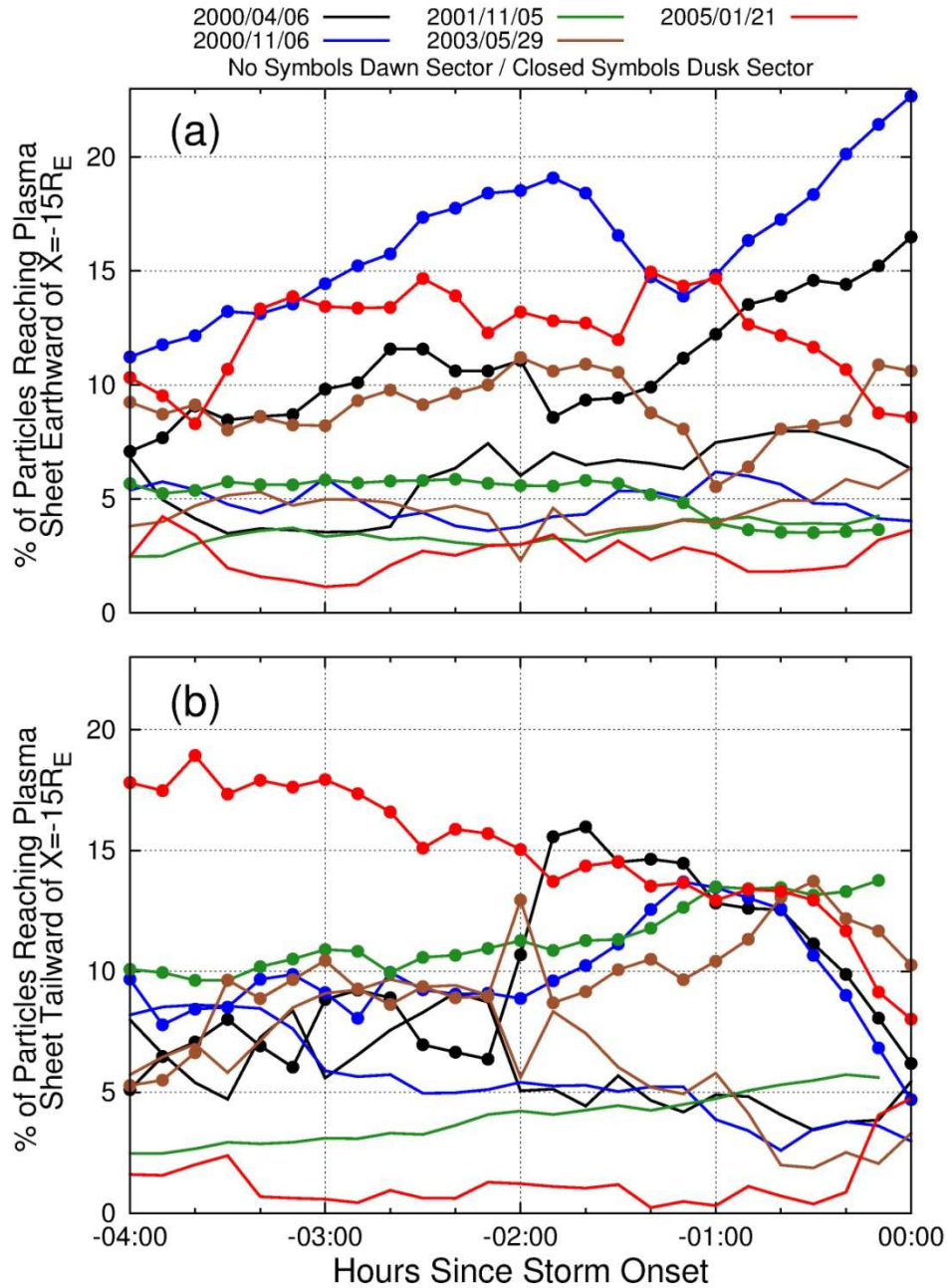


Figure 8 Percentage of un-trapped thermal-energy O^+ ions reaching the dusk (solid circles) and dawn (no circles) sectors of the (a) plasma sheet and (b) magnetotail, as a function of the launch time of the ions, 0–4 hrs before the onset of the main phase of the magnetic storms on (A) 6 April 2000 (black), (B) 6 November 2000 (blue), (C) 5 November 2001 (green), (D) 29 May 2003 (brown), and (E) 21 January 2005 (red), respectively; and 2–6 hrs before the onset on (C) 5 November 2011 with the data display shifted to the right by 2 hours in the figure.